

Article

Mesoporous Magnetic Cysteine Functionalized Chitosan Nanocomposite for Selective Uranyl Ions Sorption: Experimental, Structural Characterization, and Mechanistic Studies

Ahmed A. Al-Ghamdi ¹, Ahmed A. Galhoum ², Ahmed Alshahrie ^{1,3}, Yusuf A. Al-Turki ^{4,5}, Amal M. Al-Amri ⁶ and S. Wageh ^{1,*}

¹ Department of Physics, Faculty of Science, King Abdulaziz University, Jeddah 21589, Saudi Arabia; agamdi@kau.edu.sa (A.A.A.-G.); aalshahri@kau.edu.sa (A.A.)

² Nuclear Materials Authority, El-Maadi, Cairo P.O. Box 530, Egypt; galhoum_nma@yahoo.com

³ Centre of Nanotechnology, King Abdul-Aziz University, Jeddah 21589, Saudi Arabia

⁴ Department of Electrical and Computer Engineering, Faculty of Engineering, King Abdulaziz University, Jeddah 21589, Saudi Arabia; yaturki@yahoo.com

⁵ K. A. CARE Energy Research and Innovation Center, King Abdulaziz University, Jeddah 21589, Saudi Arabia

⁶ Physics Department, Rabigh College of Science and Arts, King Abdulaziz University, P.O. Box 344, Rabigh 21911, Saudi Arabia; amsalamri@kau.edu.sa

* Correspondence: wswelm@kau.edu.sa



Citation: Al-Ghamdi, A.A.; Galhoum, A.A.; Alshahrie, A.; Al-Turki, Y.A.; Al-Amri, A.M.; Wageh, S. Mesoporous Magnetic Cysteine Functionalized Chitosan Nanocomposite for Selective Uranyl Ions Sorption: Experimental, Structural Characterization, and Mechanistic Studies. *Polymers* **2022**, *14*, 2568. <https://doi.org/10.3390/polym14132568>

Academic Editor: Deng-Guang Yu

Received: 15 May 2022

Accepted: 20 June 2022

Published: 24 June 2022

Publisher's Note: MDPI stays neutral with regard to jurisdictional claims in published maps and institutional affiliations.



Copyright: © 2022 by the authors. Licensee MDPI, Basel, Switzerland. This article is an open access article distributed under the terms and conditions of the Creative Commons Attribution (CC BY) license (<https://creativecommons.org/licenses/by/4.0/>).

Abstract: Nuclear power facilities are being expanded to satisfy expanding worldwide energy demand. Thus, uranium recovery from secondary resources has become a hot topic in terms of environmental protection and nuclear fuel conservation. Herein, a mesoporous biosorbent of a hybrid magnetic–chitosan nanocomposite functionalized with cysteine (Cys) was synthesized via subsequent heterogeneous nucleation for selectively enhanced uranyl ion (UO_2^{2+}) sorption. Various analytical tools were used to confirm the mesoporous nanocomposite structural characteristics and confirm the synthetic route. The characteristics of the synthesized nanocomposite were as follows: superparamagnetic with saturation magnetization (M_S : 25.81 emu/g), a specific surface area (S_{BET} : 42.56 m²/g) with a unipore mesoporous structure, an amine content of ~2.43 mmol N/g, and a density of ~17.19/nm². The experimental results showed that the sorption was highly efficient: for the isotherm fitted by the Langmuir equation, the maximum capacity was about 0.575 mmol U/g at pH range 3.5–5.0, and Temperature (25 ± 1 °C); further, there was excellent selectivity for UO_2^{2+} , likely due to the chemical valent difference. The sorption process was fast (~50 min), simulated with the pseudo-second-order equation, and the sorption half-time ($t_{1/2}$) was 3.86 min. The sophisticated spectroscopic studies (FTIR and XPS) revealed that the sorption mechanism was linked to complexation and ion exchange by interaction with S/N/O multiple functional groups. The sorption was exothermic, spontaneous, and governed by entropy change. Desorption and regeneration were carried out using an acidified urea solution (0.25 M) that was recycled for a minimum of six cycles, resulting in a sorption and desorption efficiency of over 91%. The as-synthesized nanocomposite's high stability, durability, and chemical resistivity were confirmed over multiple cycles using FTIR and leachability. Finally, the sorbent was efficiently tested for selective uranium sorption from multicomponent acidic simulated nuclear solution. Owing to such excellent performance, the Cys nanocomposite is greatly promising in the uranium recovery field.

Keywords: mesoporous magnetic chitosan nanocomposite; cysteine; uranyl ions; mechanistic studies; XPS; uptake kinetics and sorption isotherms

1. Introduction

Uranium is the most significant element for nuclear energy production, but it is a limited resource, and a shortage is projected in the near future. It is also highly toxic. The extraction of uranium and the development of nuclear power can produce hazardous and

radioactive waste [1–5]. Consequently, uranium separation and recovery are important processes in terms of both uranium resource exploitation and environmental preservation. Sorption (sometimes called solid-phase extraction) is a promising method for recovering metal ions from dilute effluents, due to its low environmental impact, quick kinetics, excellent selectivity, ease of handling, and great efficiency [2,6–9]. Recent progress in uranium(VI) ion sorption from contaminated water has been conducted using various sorbents such as organic materials, e.g., cellulose/chitosan-based sorbent materials [1–5], functionalized synthetic polymers [1,10], hydrogel [11], and aerogel [12]. Moreover, porous materials have been widely studied in the field of uranium extraction from seawater [1–3]. Clays, metal oxides, and AL-based LDH are examples of inorganic materials [13]. Magnetic nanocomposites, as well as nanomaterials, are examples of composite and metal–organic frameworks (MOFs) [2,14].

As an alternative to traditional synthetic resins, biosorption and biopolymers such as chitosan and cellulose have recently attracted a lot of attention [1–5]. For water remediation, chitosan-based polymers have been widely investigated [15–17]. Chitosan (CT), a reactive biopolymer (amino-polysaccharide obtained by alkaline acetylation of chitin), has received great attention because it is a renewable resource, abundant, and biodegradable [1–5]. CT is a good sorbent for metal ions, and bears hydroxyl and amine reactive functionalities that can be bound in a variety of mechanisms: metal anions are attracted to each other through ion exchange/electrostatic attraction, and metal cations are chelated [1–5], and open up a world of further functionalization. Chitosan appears to be a good starting material for chelating resin production [8,18]. Resistance to mass transfer is frequently the key limiting phase in sorption processes. The difficulty is to increase porosity or use small-size materials at the expense of more complicated solid/liquid separation at the sorption equilibrium [10,19].

Magnetic-based composites can overcome this disadvantage. Nanocomposites are multiphase materials made up of nanometric iron oxide (Fe_3O_4) particles incorporated in a polymer matrix [17]. This is the approach taken in the current study to develop a new sorbent for uranium recovery [1–5]. The art of building innovative multiphase nanomaterials for efficient uranium sorption involves the fabrication of an organic–inorganic functional hybrid nanocomposite (high capacity and selectivity). Furthermore, an external magnetic field can be used to recover and collect the sorbents [5,20]. This is the main reason for the manufacture of magnetic sorbent synthesis based on chitosan. Grafting diverse reactive functional groups enhances sorption capacity, target metal selectivity, and the pH range for efficient sorption [1,19]. Several chelating ligands can be used for the sorption of uranium ions, such as catechol, iminodiacetic acid [1–5], aminophosphonate (acids and esters) [3,8], polyamines [21], magnetic Schiff's base chitosan composite [21], phenylarsonic acid and amino acid moieties functionalized crosslinked chitosan [1–5], and tryptophan-porous organic polymer [22]. Amino acids are chemical organic compounds rich with amine ($-\text{NH}_2$) and carboxylic acid ($-\text{COOH}$) (i.e., considered as hard bases), as well as a side chain (e.g., $-\text{OH}$, $-\text{SH}$), and have a strong affinity for uranium (hard acid), according to Persson's definition of the HSAB hypothesis [1–5].

To date, no articles have reported the extensive and deep characterization needed for mechanistic studies of the synthesis procedures, chemical modification, sorption, and desorption mechanism for uranyl ions. Therefore, it is highly desirable to develop an extensive discussion of these points. Thus, herein, a co-precipitation of a magnetic nanoparticle coating with a thin film layer of chitosan was conducted, resulting in a magnetic chitosan nanocomposite, which was followed by further modification with cysteine via a continuous reaction. The physicochemical characteristics were characterized by elements analysis, XRD, pHpzc, TEM, VSM, FTIR, and XPS. The magnetic chitosan nanocomposite formation and cysteine grafting mechanism are discussed in detail. Experimental results and spectroscopic (FTIR and XPS) studies were used to predict the uranium surface complexation models. Sorption of UO_2^{2+} onto the Cys nanocomposite as functions of sorbent dose, pH, contact time, uptake kinetics, sorption isotherms, thermodynamic characterization, and

selectivity was analyzed. Further, the sorbent regeneration and re-usability were examined. Finally, mechanistic studies of the nanocomposite formation (magnetite preparation and chemical modification stages), sorption, and desorption were studied and are discussed in detail.

2. Materials and Methods

2.1. Materials

Chitosan (DD: 93%) was supplied by Acros Organics. Epichlorohydrin (CAS:106-89-8), 1,4-dioxane (CAS: 123-91-1), Cysteine (CAS: 52-90-4), Arsenazo III (A.R. grade), $\text{FeCl}_2 \cdot 4\text{H}_2\text{O}$ ($\geq 99\%$), and FeCl_3 ($\geq 99.99\%$) were provided from Sigma-Aldrich. All reagents were used exactly as they were given without any purification. Uranyl acetate ($\text{UO}_2(\text{OCOCH}_3)_2 \cdot 2\text{H}_2\text{O}$) (Sisco Research Laboratories Pvt. Ltd., Mumbai, India) was dissolved in ultrapure water to prepare a stock solution (1000 mg U/L). Uranium content was analyzed using a UV/Vis spectrophotometer [23].

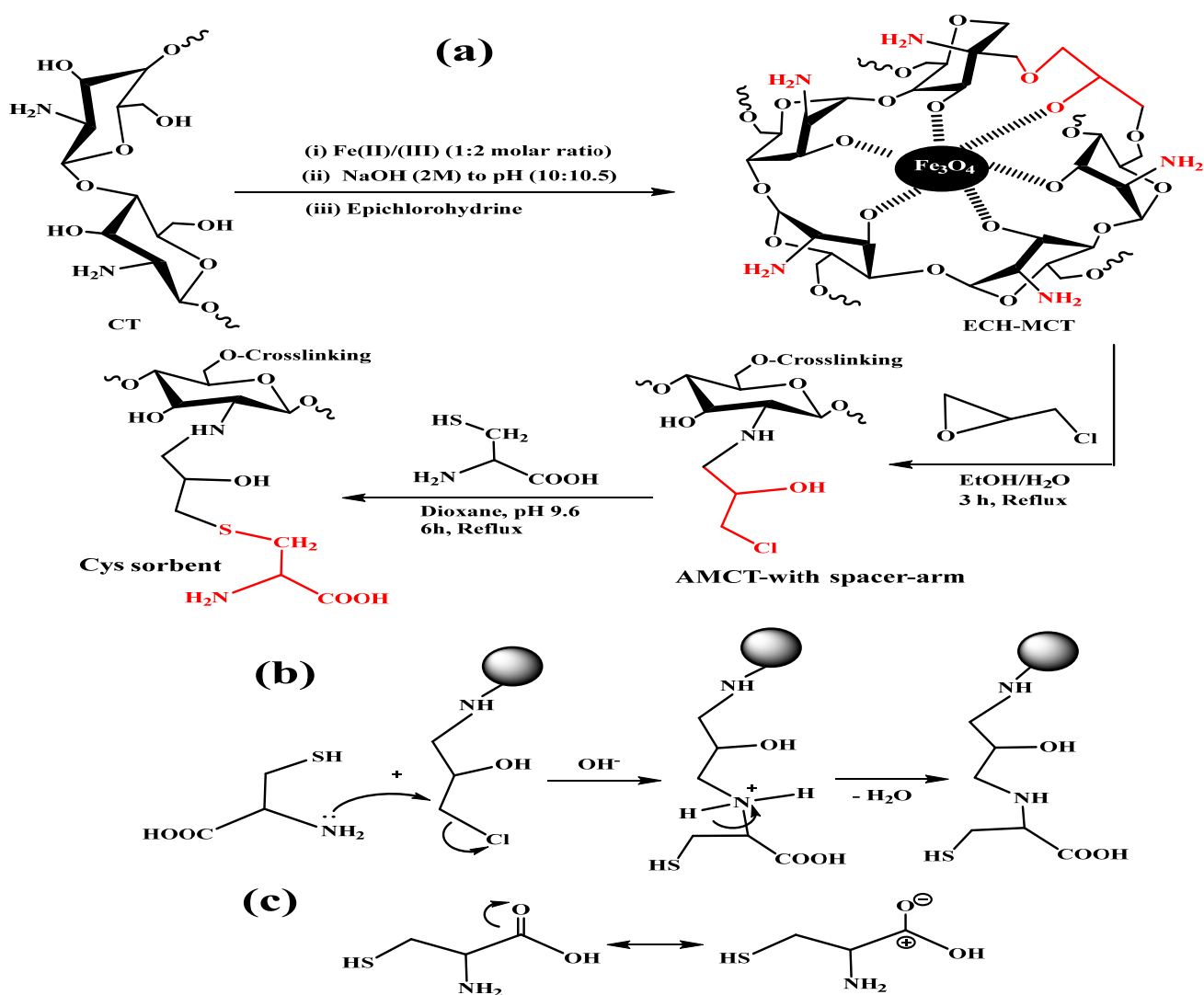
2.2. Sorbent Synthesis

2.2.1. Chitosan–Magnetite Nanocomposite Preparation

A hybrid magnetic chitosan nanocomposite was created by hydrothermally co-precipitating Fe^{II} and Fe^{III} mixture with NaOH in the presence of chitosan in a one-step process [4,5]. Chitosan powder (2 g) was steeped and dissolved in acetic acid solution (200 mL, 5% *w/w*) with ferrous chloride (FeCl_2 , 2.42 g) and ferric chloride (FeCl_3 , 3.82 g) (1:2 molar ratio, respectively). At 40–45 °C, the mixture solution was precipitated by adding NaOH (2 M) dropwise with steady stirring at pH 10.5–11. The suspension was heated for 1 h at 90 °C while stirring constantly, and the particles were magnetically collected. The freshly magnetic chitosan nanocomposite was chemically enhanced by crosslinking with an epichlorohydrin solution (0.01 M) at 1:1 mass ratio under alkaline conditions (pH ~ 10) [6]. The suspension mixture was heated at 50 °C for 2 h with constant stirring. At the end, the cross-linked magnetic chitosan nanocomposite was magnetically collected and washed extensively with ethanol/water to eliminate any unreacted reagent.

2.2.2. Nanocomposite Functionalization

Cysteine was functionalized with cross-linked magnetic chitosan nanocomposite as depicted in Scheme 1 using a generic approach. The cross-linked magnetic chitosan nanocomposite was suspended in aqueous ethanol solution (75 mL, 1:1 in *v/v*) before 10 mL of epichlorohydrin was added; refluxing the mixture at 65–70 °C for 3 h yielded the desired results [7]. The product was filtered and rinsed thoroughly with ethanol and ultrapure water. Finally, the activated product and cysteine (8 g) were suspended in 100 mL of dioxane, and the mixture pH was adjusted to 9.5–10. The mixture was refluxed at 95 °C for 8 h. The final product was magnetically separated and washed extensively with ethanol and ultrapure water. The sorbent was finally freeze-dried.



Scheme 1. Synthesis of Cysteine–modified magnetic chitosan nanocomposite (a), and revised process for cysteine grafting via SN2 mechanism (b,c).

2.3. Characterization

(C, H, N, and S) was determined using an automatic analyzer (CHNS Vario EL III–elementar analyzer, Elementar, Langensfeld, Germany). A Philips X–ray generator type PW 3710/31, Cu K α ($\lambda = 1.544$) (Philips model, Eindhoven, The Netherlands) was used to measure X–ray diffraction. The FTIR spectra were analyzed by a Thermo-Fisher Nicolet IS10 spectrometer (Waltham, MA, USA). The morphology and size distribution were analyzed by TEM-JEOL-2100 transmission electron microscope (JOEL, Tokyo, Japan). The magnetic characteristics were determined using a vibrating sample magnetometer (VSM; 730T, Lakeshoper Cryotronics, inc., Westerville, OH, USA). A Quantachrome NOVA 3200 (Boynton Beach, FL, USA) analyzer was used to measure the surface area using N₂-adsorption isotherms under a degassing temperature of 40 °C for 12 h, while the pore volume was measured according to the BJH method. The K-Alpha spectrometer (Thermo Fisher Scientific, Waltham, MA, USA) was used to acquire X–ray photoelectron spectroscopy (XPS) data using a monochromatic Al K α -radiation source (200 W). The sorbent's pH point of zero charge (pH_{PZC}) was measured using the pH–drift method [7,8], and the sorbent was equilibrated for 24 h under agitation with a series of 0.1 M NaCl solutions with different initial pH-values (pH₀); the equilibrium pH (pH_{eq}) was recorded, and the pH_{PZC} was the pH at which $\Delta\text{pH} = 0$.

2.4. Batch Sorption and Desorption Experiments

The sorption properties of synthesized sorbent were investigated. A constant UO_2^{2+} solution volume (20 mL) with a definite concentration (C_0 , mmol U/L) was agitated and equilibrated with a given amount of sorbent (10 mg) for 180 min at room temperature (298 ± 1 K), 200 rpm and initial pH (pH_0 4.0), except when the following were present: the effect of initial pH (the pH_0 : 1.3–5.5), equilibration time (from 0 min to 150 min. at pH_0 : 4.0), isotherm at various concentrations (C_0 : 0.21–1.26 mmol U/L), temperature (at 298 – 328 ± 1 K), and sorbent dose (SD: 0.25–1.5 g/L) on the sorption capacities. After equilibrium and phase separation, the initial, residual UO_2^{2+} concentration at equilibrium and at different interval times (C_0 , C_{eq} , and C_t : mmol U/L) were determined by the Arsenazo III method (using a double beam UV-11601, UV-Vis spectrophotometer (Shimadzu Corporation, Kyoto, Japan)). The sorption capacity (q_{eq} , mmol U/g) was evaluated by the mass balance equation and the distribution coefficient (D : $q_{\text{eq}}/C_{\text{eq}}$) in L/g, as shown in Equations (1) and (2), respectively:

$$q_{\text{eq}} = \frac{(C_0 - C_{\text{eq}}) \times V}{m} \quad (1)$$

$$D = \frac{(C_0 - C_{\text{eq}})}{C_0} \times \frac{V}{m} \quad (2)$$

where m (g) is the amount of sorbent, and V (L) is the solution's volume. Experimental conditions are stated in the figure captions: in most cases, the equilibrium time was 50 min (at room temperature, i.e., 298 K), and the pH_0 was set at 4.0. All values are means of duplicated with standard deviation ± 4 –5%.

The influence of competing cations on the uranyl sorption in a synthetic simulated nuclear industry effluent was studied in order to explore the selectivity toward U(VI). A standardized investigation was conducted utilizing some of the most common metals present in nuclear industry effluents, such as REs(III): La, Ce, Eu, and Yb, and other co-ions (Co, Cd, Cs, Sr, and Ba). Equimolar multi-solutions (as the saline content of nuclear industry wastewater is usually considerable) were made for this investigation using their nitrate and chloride salts. The sorption studies were conducted at room temperature (298 ± 1 K), and with a 0.5 g/L sorbent dose for 60 min and agitation (200 rpm). After filtration, the remaining concentrations were determined by atomic absorption spectrometry (AAS: a Solar Unicam 969, Thermo Scientific, USA) for Co, Cd, Cs, Sr, and Ba, and uranium and rare earth ions were determined by ICP spectrometry (ICP-OES, Prism ICP, Teledyne Leeman Labs., Hudson, NH, USA).

The optimization of the regeneration/recycling (for six successive sorption/desorption cycles) of the sorbent was conducted using acidified urea (10 mL, 0.5 M) with a fixed sorbent weight (10 mg). The contact time was set to 30 min at 200 rpm and at 298 ± 1 K. At each phase, the sorption and desorption efficiency for six cycles were evaluated and compared to the value reached for the first cycle. The equations that describe desorption efficiency (D_E), and regeneration efficiency (RE) are Equations (3) and (4), respectively:

$$D_E = \frac{C_D \times V_L \times 100}{m_d \times q_d} \quad (3)$$

$$\text{RE} = \frac{q_d \times 100}{q_e} \quad (4)$$

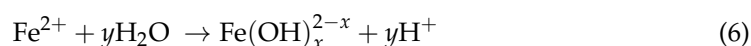
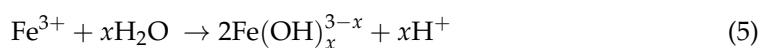
where q_d (mmol U/g) is the sorption capacity before first desorption, C_D (mmol U/L) is the U concentration in the eluate, V_L is the volume of the eluent, q_e (mmol U/g) is the sorption capacity at the first cycle and m_d (g) is the amount of sorbent employed in the desorption stage.

3. Results and Discussion

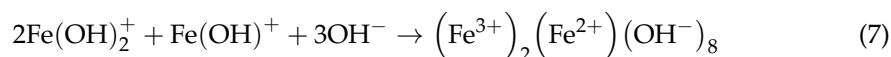
3.1. Basics of Hybrid Nanocomposite

A magnetic chitosan nanocomposite was synthesized by heterogeneous nucleation via a hydrothermal one-step co-precipitation of Fe^(II) and Fe^(III) ions using NaOH in the presence of chitosan at pH ~ 10.5. First, Fe₃O₄ nanocrystals were used for nucleation of the chitosan film layer from the solution [4]. The simple overall reaction for synthesizing non-magnetic (Fe₃O₄) nanoparticles under alkaline conditions was conducted using different bases, BOH (B⁺: NH₄⁺/Na⁺/K⁺). The reaction of Fe^{(II)/(III)} precursor solution and the precipitant base (BOH) was slightly exothermic. The iron oxide (ferrous–ferric oxide (FeO/Fe₂O₃)) particle formation started as soon as NaOH was added into the iron salts. The hydrolysis products Fe(OH)⁺ and Fe(OH)₂⁺ interacted to form ferrihydrite, which preferentially precipitated (Fe(OH)_{2(s)} ↔ Fe(OH)_(aq)⁺ + OH[−]) and turned into magnetite (Fe₃O₄), which was formed as a result of thermodynamic instability [9], as the following mechanism shows (Equations (5)–(11)) [9,21].

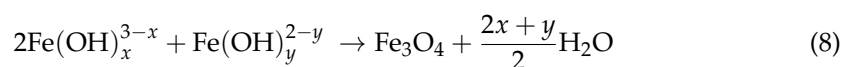
Deprotonation step:



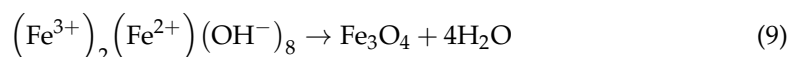
Ferrihydrite intermediate production:



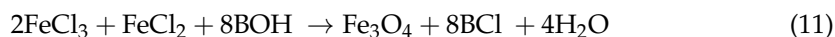
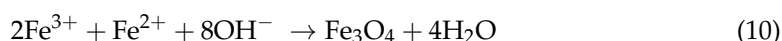
Oxidation and dehydration step:



Magnetite is formed when ferrihydrite dehydrates:



Overall reaction:



This reaction took place under N_{2(g)}, to prevent Fe^(II) from oxidizing to Fe^(III). The magnetite can be oxidized to other ferric hydroxide phases, e.g., maghemite by the ion transfer process (Fe₃O₄ + 2H⁺ → γ-Fe₂O₃ + H₂O + Fe²⁺) [21], goethite (α-FeOOH), and sometimes hematite (4Fe₃O₄ + 4O₂ → 6Fe₂O₃) [21,24]. To avoid both dissolving in acidic environments, magnetite–chitosan nanocomposites are cross-linked using epichlorohydrin, and sorption capacity loss is prevented when amine groups are included (i.e., aldehyde crosslinking is used) [7]. Further, the crosslinking unfunctional agent is employed to generate covalent connections with the C-atoms attached to chitosan's hydroxyl groups (related to the epoxide ring rupture and a chlorine atom being released) [5].

The synthesis of the magnetic-cysteine-functionalized chitosan nanocomposite is depicted in Scheme 1a. Finally, in alkaline dioxane solution and heating, a typical substitution nucleophilic bimolecular (SN₂) reaction occurs between nucleophilic sites on the cysteine moiety (in terminal –NH₂ and/or –SH) and the carbon linked with the Cl element, and is considered to be responsible for the chemical reaction/modification. The alkaline aprotic solvent promotes this reaction (Scheme 1b). Carboxylic groups are electron withdrawing sites that help to remove the lone electron pair on the N-atom from cysteine, making them less nucleophilic (Scheme 1c): this might explain possibility of –SH groups are preferred

over $-\text{NH}_2$. However, the strength of $-\text{NH}$ stretching vibration increased significantly in the FTIR spectra, but free $\text{C}-\text{S}$ stretching vibration was observed at 742 cm^{-1} [10]. Although several amino groups of the amino acid may be implicated in immobilization, it appears that the majority of grafting occurs via the alternative substituent via $-\text{SH}$ sites.

3.2. Sorbent Characterization

3.2.1. Element Analysis

The elemental analysis (CHNS) of the materials (in w/w) was compared during the synthesis procedure (Table 1). When raw chitosan's (r-CT) and magnetic chitosan's (MCT) organic fractions (related to C and N elements) were compared, the weight percentage of raw chitosan was found to be significantly lower ($\sim 52.7\text{--}53.9\%$): this is related to the presence of iron oxide (Fe_3O_4) nanoparticles. The organic fraction was $\sim 46.5\%$, whereas magnetite accounted for $\sim 53.5\%$ of the total weight, which was consistent with the mass balance experiments. Surprisingly, the increase in the mass of the magnetite chitosan nanocomposite was about 5.35 g compared to the theoretical calculation (4.0 g), based on the initial chitosan to magnetite weight ratio (2 g:2 g). After the crosslinking step, the N-content (mmol%) of cross-linked magnetic chitosan (CMCT) decreased from 2.56 to 2.17, due to increasing epichlorohydrin binding (N-atoms; thus, N-content decreased in the final products), which was consistent with the slight reductions in the C and H contents. Meanwhile, after the activation and insertion of the terminal $-\text{Cl}$ atom via epichlorohydrin reaction, the molar mass of activated magnetic cross-linked chitosan (AMCT) steadily increased; therefore, the C, H, N contents were "diluted", and the changes in the weight percent ($\Delta\text{wt.}, \%$) were 10.8, 14.4, and 18.3%, respectively. By analogy, a similar result was observed from immobilizing Cl atoms by the reaction of thionyl chloride (SOCl_2) for the subsequent immobilization of amine-bearing moieties. After chlorination, the fraction of C and H elements strongly decreased by about 21.8% and 24.5%, respectively, as a result of the Cl atom influence on the final product [12]. Finally, after cysteine grafting, the S content (wt., %) of the obtained Cys nanocomposite (Cys) reached 3.01% (0.94 mmol S/g) and the increases in the C, H and N contents clearly showed the successful synthesis process. The effective amino contents before and after cysteine grafting were about 1.41 and 2.43 mmol U/g, respectively, i.e., the relative ratio to the AMCT was about 1.72 times. The nitrogen content of the nanocomposite was 2.43 mmol N/g ($\sim 3.40\text{ }w/w$). The amine groups in r-CT were $\sim 5.54\text{ mmol N/g}$. This indicates that the magnetite fraction was about $50 \pm 10\%$.

Table 1. Elemental analysis of nanocomposite synthesis stages.

Materials	C (%)	H (%)	N (%)	N (mmol/g)	S (%)
r-CT	39.97	6.86	7.76	5.54	—
MCT	18.91	4.07	3.58	2.56	—
CMCT	18.35	3.93	3.01	2.15	—
AMCT	15.82	3.23	1.98	1.41	—
Cys	20.51	4.01	3.40	2.43	3.01

The symbolical amine density (=the number of amine molecules/specific surface area (in nm^2/g)) was about 17.19 for Cys and 713.74 for r-CT (S_{BET} : $4.56\text{ m}^2/\text{g}$ for particle size $\leq 100\text{ }\mu\text{m}$). The N and magnetite contents showed a large dispersion, likely due to the insertion of other atoms. The theoretical content took into consideration the amount of organic reagents used during the synthesis steps.

3.2.2. pH Point of Zero Charge (pH_{PZC}) by Drift Titration Method

Figure 1a reports the titration profiles of MCT and Cys, which were consistent with these successive steps. The pH_{PZC} , which corresponded to $\Delta\text{pH} = 0$, was hardly changed by cysteine grafting on magnetic chitosan: 7.29 ± 0.02 and 7.78 ± 0.02 was recorded for MCT and Cys, respectively. The pH_{PZC} of the MCT particle was affected by the Fe_3O_4 core: it was close to 7.29. This was lower than the pH_{PZC} of r-CT: 8.52, and is in line with the pK_a value

of 6.3–6.6 for the $-\text{NH}_2$ groups of chitosan biopolymer [13,20]) due to the charge density, screening effect, and amount of impeded Fe_3O_4 [20]. After cysteine grafting, the pH_{PZC} increased to 7.78 ± 0.02 . This can be easily explained by the immobilization of additional amine, carboxylic acid, and thiolate ($-\text{S}$) groups. The pK_a values of cysteine were 1.71 and 7.85 for the $-\text{COOH}$ group and $-\text{NH}_2$ group, respectively [14], while the cysteinyl thiol group has been found to have different pK_a values of 6.4–7.4 [19]. The grafting of cysteine onto the activated magnetite–chitosan nanocomposite appeared to make the net results of all the acid–base properties of the composite (pH_{PZC} : 7.78 ± 0.02) closer to the cysteine’s amine moiety against the carboxylic group end.

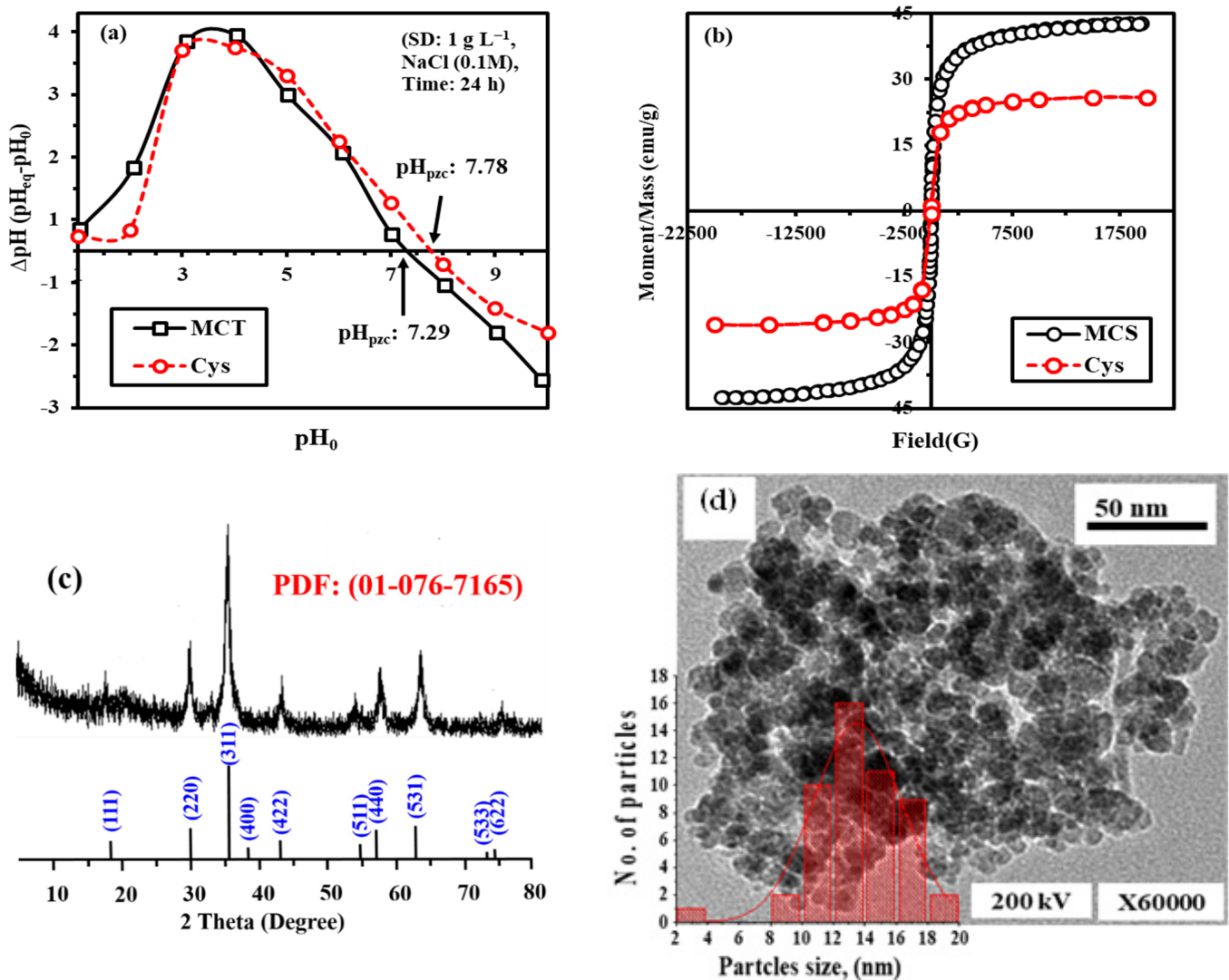


Figure 1. (a) Determination of pH_{PZC} by the pH-drift method; (b) Magnetization curves of MCT and Cys; (c) XRD patterns of Cys (the bar-type spectrum represents the XRD referenced pattern of magnetite); and (d) TEM micrographs (the bar is 50 nm).

3.2.3. Magnetic Properties

The magnetic curves of MCT and Cys were recorded and compared using VSM at room temperature (Figure 1b). Obviously, both samples were superparamagnetic and characterized with no hysteresis loop or remanence and coercivity. The MCT magnetic saturation (M_s) was 42.53 emu/g; however, the raw MCT functionalization (cysteine grafting) reduced the M_s to 25.81 emu/g. The M_s values obtained were substantially lower than those recorded from bulk magnetite NPs (~ 80 emu/g) [25]). For raw MCT, M_s fell below 42.53 emu/g: magnetite NPs immobilized in polymer matrices showed comparable

reductions [25]. The molecular weight of the polymer coating increased according to $MCT < Cys$, which suggests that the proportion of Fe_3O_4 core in the composite reduced in lockstep with the fall in M_s values [4,25]. Moreover, the M_s values related to the Fe_3O_4 amounts in the MCT and Cys were about 56% and 47%, respectively, from the elemental and mass balance analysis results; the chemical modification increased the organic film thickness and resulted in decreases in the magnetic properties. However, these M_s values were adequate for facile and effective magnetic separation from the aqueous media.

3.2.4. XRD

The XRD pattern of Cys, which is displayed in Figure 1c, showed eight well-defined diffraction peaks at $2\theta = 19^\circ, 30^\circ, 35^\circ, 43^\circ, 54^\circ, 57^\circ, 62^\circ,$ and 74° , which were indexed to the (111), (220), (311), (400), (422), (511), (440), and (533) planes, respectively. The Fe_3O_4 cubic spinel structure is shown by the XRD pattern [26]. However, the potential of maghemite (Fe_2O_3) coexisting with ferromagnetic characteristics cannot be ruled out. From XPS, the Fe 2p band on the sorbent spectrum can be deconvoluted into three signals (each with its own doublet signal) related to $Fe^{(III)}$ under both octahedral and tetrahedral forms, and $Fe^{(II)}$ (octahedral form). The resolution of the relevant satellite bands was poor. The Fe 2p_{3/2} signal, which was located at 710.6 eV, might have been delegated to the most common types of iron oxides, e.g., Fe_3O_4 or $\gamma\text{-}Fe_2O_3$ (maghemite) compounds [18]. The size was estimated to be around 12.7 nm using the highest and strongest peak matching to the (311) index (applying the Scherrer equation). This size was systematically (<20 nm) reported for enhanced superparamagnetic character.

3.2.5. TEM Analysis

Figure 1d displays the TEM micrographs of the Cys nanocomposite. The Fe_3O_4 nanoparticles appeared as spherical dense dots, surrounded by bright areas, which represent the polymeric shell (due to the electron-absorbing disparities between organic and inorganic components [25]). The nanocomposite had a regular spherical structure, well proportioned, and were apparently mono-dispersed. However, iron oxide nanoparticles (Fe_3O_4 NPs) have a tendency to aggregate, owing to magnetic interaction between dipoles/dipoles [5]. This confirmed the successful incorporation of the nanoparticles into the polymeric matrix. The aggregation verified the high magnetism, which corresponded to magnetism measurements. The particle size observed on the TEM images was used to visualize the actual size of the Fe_3O_4 NPs. Image software was used to obtain the size distribution histograms counting at least 50 particles, and the average particle size was found to be 14.01 ± 3.7 nm with a narrow particle size distribution (Figure 1d), which was consistent with the XRD results. The size of the Fe_3O_4 particles remained <20 nm; this supports the theory that the sorbent can be classified as a nanocomposite.

3.2.6. Textural Properties

The textural properties of the synthesized Cys nanocomposite were evaluated using the BET equation, which was used to calculate the specific surface areas. Additionally, the pore volume and pore diameter were deduced from N_2 -adsorption-desorption isotherms. The isotherm profile was the type II form, which were classified as nonporous materials according to the Langmuir classification, and they had a wide distribution of pore sizes (Figure 2). The specific surface area was $42.56 \text{ m}^2/\text{g}$, the porous volume was close to $0.11 \text{ cm}^3 \text{ STP}/\text{g}$, and the average pore size was ~ 3.82 nm (i.e., pore radius $DV(r): 19.09 \text{ \AA}$) with a mono-modal (i.e., uniporous) structure distribution. This indicates that the nanocomposite is a mesoporous in nature. BET analysis showed that SSA_{BET} was $\sim 42.56 \text{ m}^2/\text{g}$: this is about 20–30 times the normal value for chitosan flakes, which is consistent with natural and synthesized magnetite values [27]. This value is significantly lower than that expected for nanoparticles: this suggests that the chitosan-based material did not completely cover all iron magnetic nanoparticles. This matches the TEM finding of a thin film of chitosan coating the iron core.

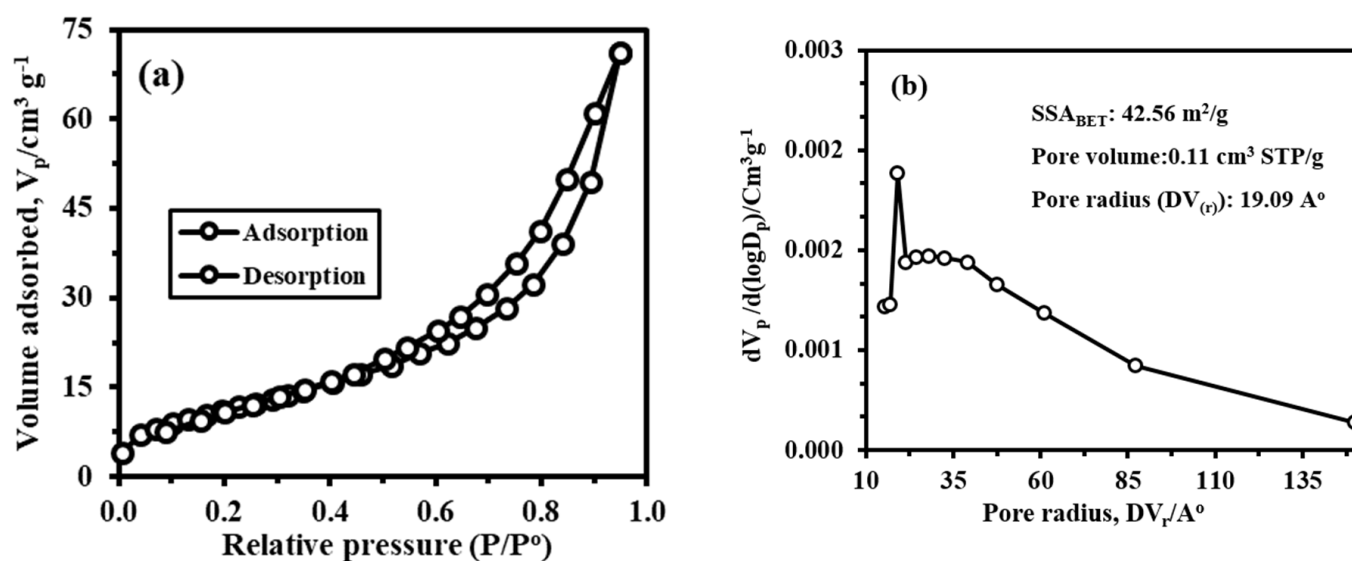


Figure 2. Textural characterization of Cys nanocomposite pore size analysis—N₂ adsorption/desorption isotherms (a) and pore-size-distribution (b).

3.2.7. FTIR Analysis

The functional groups present on the surface of the Cys nanocomposite were identified using FTIR spectrum (Figure 3). Several common bands can be identified. The band at 568 cm⁻¹ corresponded to the $\nu(\text{Fe-O})$ lattice stretching vibration of magnetite (Fe₃O₄) nanoparticles [4]. These two bands were the result of a split in the ν_1 of the bulk Fe₃O₄ ($\nu(\text{Fe-O})$) at 568 cm⁻¹, as well as the observed band at ~423 cm⁻¹, which was the blue-shift of the bulk magnetite's ν_2 (Fe-O bond) [22]. A strong and broad absorption band at 3402 cm⁻¹ can be attributed to overlapped bands for -OH and -NH stretching vibrations, as well as polysaccharide hydrogen bonds [22]. The high-intensity peaks in 2916, 2873, and 1384 cm⁻¹ were assigned to C-H stretching vibration (CH₂ at C-6, symmetric and asymmetric) and C-H bending, respectively [7,28]. The significant peak at 1628 cm⁻¹ can be attributed to N-H bending vibration (-NH₂ and >NH amine bend-in plane deformation), as well as symmetric stretching of (COO⁻) carboxylate group grafting [5,7]. The peak around 2363 cm⁻¹ might have been due to stretching O=C=O in CO₂. The two shoulders observed at 1066 and 1032 cm⁻¹ were ascribed to C-O-C (in β -glucosidic linkage), C₃-OH, and/or that of C-C stretching vibration [22]. The bands at 1384 and 1066 cm⁻¹ were assigned to primary -OH stretching and secondary -OH stretching, respectively. The band at 884 cm⁻¹ represented the β -D-glucose unit [7,20]. The medium/wide band at 468 cm⁻¹ was attributed to the out-of-plane bending mode (C-C-N) [29]). The presence of a weak stretching vibration peak of the free C-S functional group at 742 cm⁻¹, which vanished after metal sorption, might have been due to its role in metal bonding, which implies that C-S reactive groups play an important role in UO₂²⁺ binding.

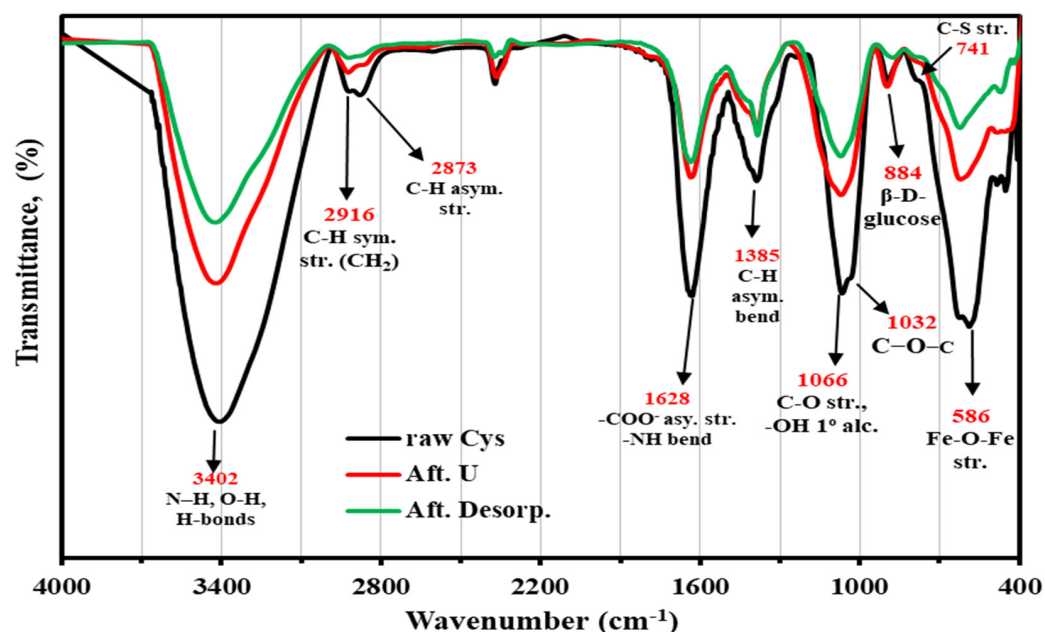


Figure 3. FTIR spectra of the Cys sorbent before and after uranium loading, and at the end of the sixth sorption/desorption cycle.

3.2.8. XPS Spectroscopy

XPS analysis was used to determine the chemical compositions of the raw nanocomposite (Cys) and after uranium sorption (Cys + U) (Figure 4). As expected, the XPS spectra of raw Cys revealed C 1s (287.7 eV), O 1s (533.2 eV), N 1s (400.9 eV), and S 2p (165.5 eV) signals before and after U(VI) complexation. The characteristic doublets of U 4f (hexavalent state) were identified by two peaks around 392.3 eV (U 4f_{5/2}) and 381.5 eV (U 4f_{7/2}), which agree well with experimental data spectra [30,31], providing direct evidence of the formation of Cys–U(VI) complexes. Moreover, there are two additional peaks attributed to U element defined as: U 4d₅ and U 4p₃. Furthermore, two peaks at 709–710 eV (Fe 2p_{3/2}) and 725–726 eV (Fe 2p_{1/2}) distinguished the magnetite (Figure S1: XPS core level spectra for main elements).

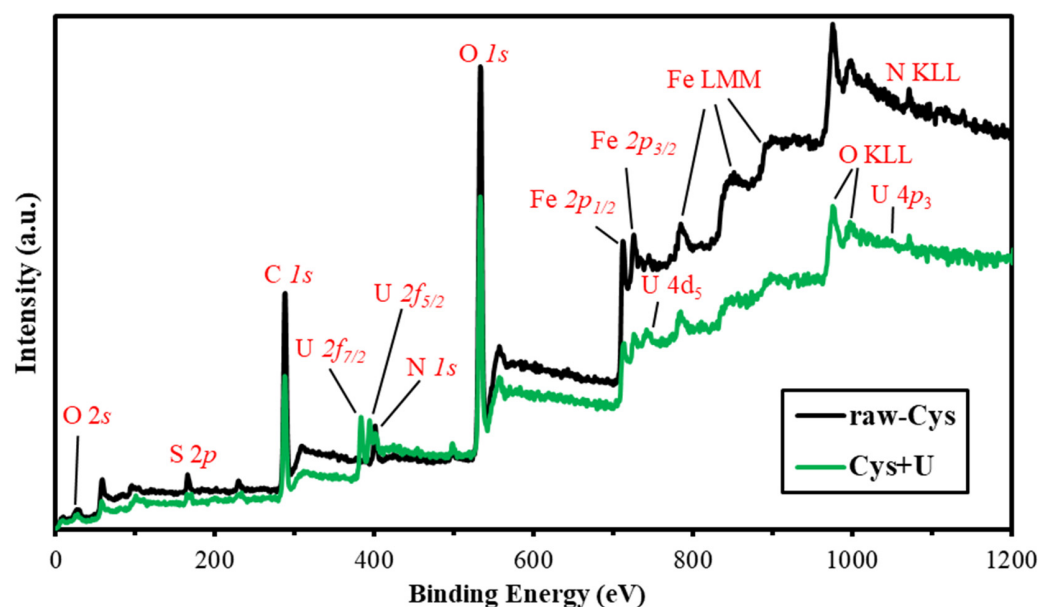


Figure 4. Cont.

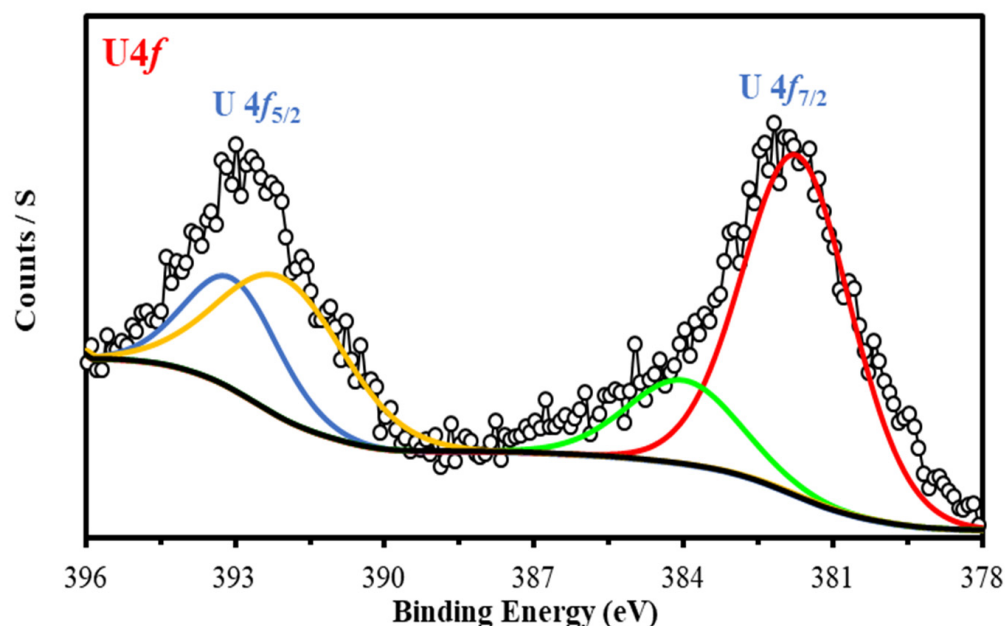


Figure 4. XPS survey spectra of raw Cys sorbent, after $U^{(VI)}$ sorption (upper panel) and core level for U 4f (lower panel).

3.3. Sorption Studies

3.3.1. Effect of Sorbent Dose

The influence of the sorbent dose (SD: 5–30 mg/20 mL) on uranyl ion sorption and removal efficiencies is shown in Figure S2. The removal efficiency improved from 5 to 30 mg/20 mL, or 0.25 to 1.5 g/L with increases in the sorbent dosage, reaching a maximum (99.5%) at 1.5 g/L; however, the sorption capacity decreased dramatically. This was likely due to the growing number of accessible binding sites. As the sorbent dose was increased, sorbent molecules partly aggregated and formed bridging bonds, reducing the effective surface area and active sites for metal ion binding [32]. Depending on the process's goal, decontamination of the effluent (lowest residual concentrations needed) necessitates a high sorbent dosage, whereas metal valorization necessitates metal concentration in the sorbent (i.e., lesser sorbent dosages). For the further experiments, a sorbent dosage of 0.5 g/L was chosen as a suitable balance between these two goals.

3.3.2. Effect of pH

Batch experiments at pH_0 : 1.3–5.5 were used to assess the pH impact. The surface charge and target metal ion speciation were determined by the solution pH [12,33]. Figure 5a demonstrates that when the initial and equilibrium pH rose, the sorption capacity increased, particularly between pH_0 1.3 and 3.0, before stabilizing at pH_0 3.0–5.0 and reaching 0.299–0.303 mmol U/g. When the pH_0 rose over pH 5.0, the sorption capacity increased slightly, most likely as a result of a shift in metal speciation: when this happens, metal ions begin to produce hydrolyzed products, resulting in a loss of affinity for amino groups, which makes ligand exchange and chelation more difficult [34]. At a lower pH, the sorbent's surface charge turned positive, and a powerful H^+ ion competed with UO_2^{2+} ions for binding sites, reducing the uranyl ion interaction [32,33]. This was confirmed by the pH_{PZC} section, which demonstrated a positively charged surface in this range at $pH_0 < 7.78$ due to the deprotonation of reactive groups. Meanwhile, as the pH increased, H^+ began to be desorbed, and the UO_2^{2+} hooked up the free binding sites. Hence, the metal sorption increased on the sorbent surface. For cross-linked magnetic chitosan (CMCT) (as a control) the sorption is still at a modest level (from 0.216 to 0.228 mmol U/g) over a wide range of pH_0 : 4.0 to 5.5 (pH_{eq} : 4.80 to 5.42), showing that Cys has a higher superiority over CMCT. This can be related to the cysteine moiety incorporation.

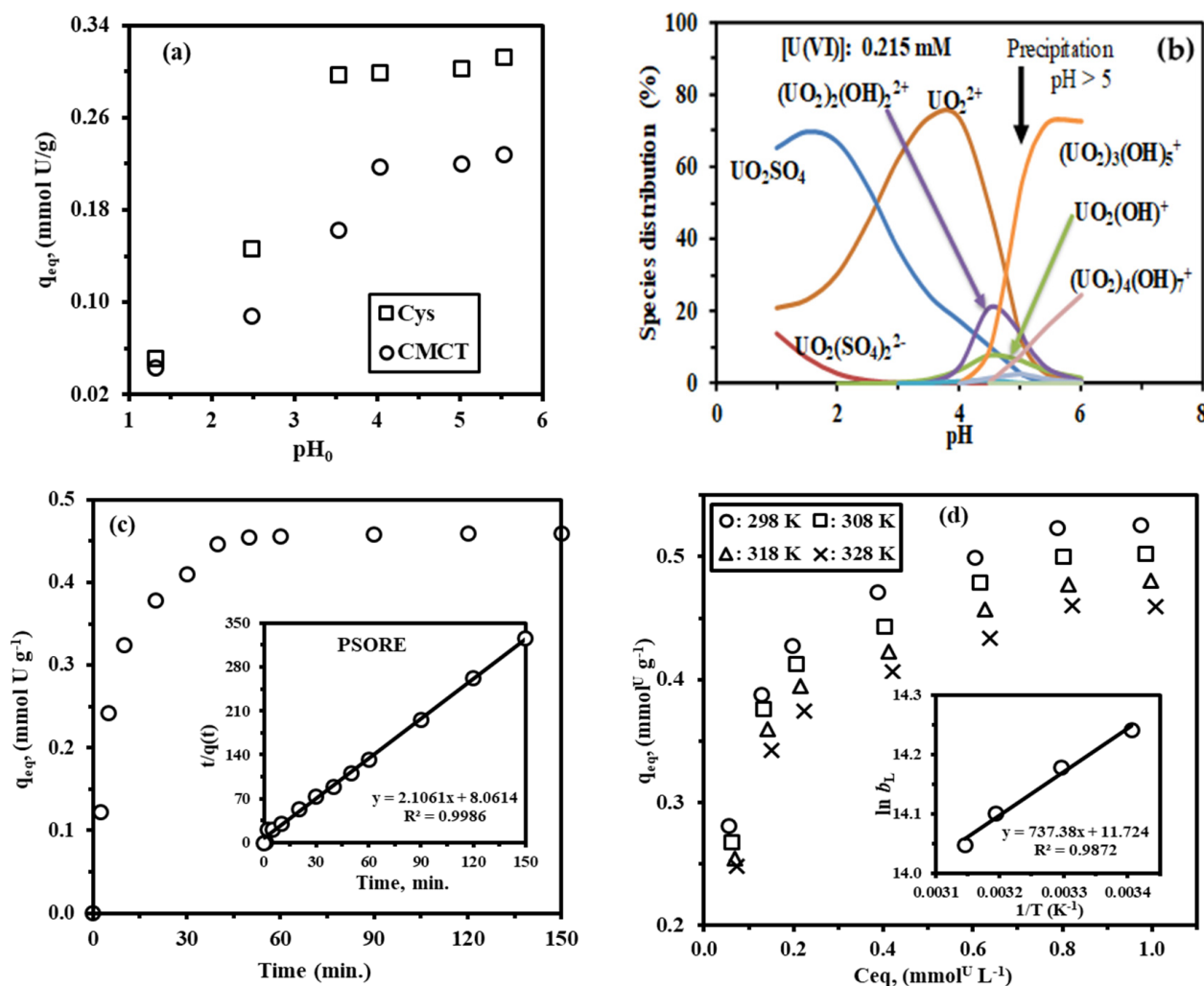


Figure 5. (a) The effect of pH on UO_2^{2+} sorption (C_0 : 0.215 mmol U/L, pH_0 : 1.3–5.5, SD: 0.5 g/L, T: 298 K, Time: 180 min, 200 rpm), (b) uranyl speciation (sulfuric acid solution) as a function of pH, calculated by using a Visual-Minted program, (c) uptake kinetics and PSORE model (C_0 : 0.43 mmol U/L, pH_0 : 4.0, SD: 0.5 g/L, T: 298 K, Time: 0.0–150 min, 200 rpm), and (d) sorption isotherms and thermodynamics: Van 't Hoff plots of $\ln b_L$ vs. $1/T$ (C_0 : 0.21–1.26 mmol U/L, pH_0 : 4.0, SD: 0.5 g/L, T: 298–323 K, Time: 60 min, 200 rpm).

Figure S2b shows the pH_0 variation after uranyl sorption. In acidic medium, the lone pair of the electron of amine groups was protonated, which can contribute to ion exchange with uranyl ion species in the sorption process. Figure S2c shows that the relationship between the $\log_{10}D$ plot and pH_{eq} was linear ($R^2 = 0.9454$ and $R^2 = 0.9761$ for Cys and CMCT, respectively), and the slope was 0.2978 and 0.2978, respectively. The line slope was connected to stoichiometric exchange with bound metal ions in ion exchange processes, indicating that the ion exchange process involving uranyl ion species is crucial [4]. Distinct processes are associated with different sorption sites depending on the initial pH_0 . The existence of carboxylic, hydroxyl, thiolate, and amine groups, with their appropriate acid–base characteristics, provide a diverse spectrum of sorbent interactions with UO_2^{2+} [5]. However, based on the distribution of the species $U^{(VI)}$ hydrolysis and polynuclear hydrolyzed uranium species (Figure 5b), uranyl ions in the suggested system will precipitate at higher pHs and initial uranium concentrations [5,20]. As a result, for further studies, an ideal pH_0 value of roughly pH: 4.0 was selected.

A multi-linearity for the relationship between plot pH_0 and q_{eq} was observed (Figure S2), implying that different stages of the mechanism occurred throughout the sorp-

tion process. The sorption process takes place in two reactions, ion-exchange (at low pH) and chelation (at slightly acidic and neutral pH) mechanisms (see above). For Cys, the first linear segment had a steep slope (" $\text{pH}_0 = 0.1107 q_{\text{eq}} + 0.1057$ " ($R^2: 0.976$), and for the second segment, the slope value was nearly relatively close to zero (" $\text{pH}_0 = 0.004 q_{\text{eq}} + 0.2828$ " ($R^2: 0.990$). This means that in the range $\text{pH}_0: 1.3\text{--}3.5$, the sorption capacities (q_{eq}) were strongly changed, while they were not changed at $\text{pH}_0: 3.5\text{--}5.0$, i.e., equilibrium (q_{eq}) is reached and stabilizes around this range. This relationship is consistent with the obtained results.

3.3.3. Equilibration Time

According to uptake kinetics, pseudo-equilibrium was attained in 50 min (under specific experimental settings) (Figure 5c). There were several phases in the process that may be identified: (a) in the rapid first stage (during the first 5 min), the sorbent removed roughly 54% of total sorption (q_{eq}); (b) the second stage (which can take anywhere between 5 and 30 min) resulted in complementary sorption, which accounted for up to 90% of total sorption; and (c) in the last slower step, at 50 min, the total percentage was 99.78%. The sorbent had mesopores large enough to allow uranium ions to pass through (Shannon radius for hydration $[\text{UO}_2(\text{H}_2\text{O})_5]^{2+}$ is 1.08 \AA [20]), which was in accordance with textural analysis. To attain the actual equilibrium, it is required to wait 50 min.

Figure S3 depicts the modelling of kinetic profiles using a simplified model of intraparticle diffusion resistance (Table S1) [35,36]. There were three linear segments, one for each of the three stages described in Figure S3. Essential characteristics are shown in Table 2. The intraparticle diffusion rate constants' values (K_{id}) for both the first and second rate constants ($K_{\text{id},1}$ and $K_{\text{id},2}$) were higher, and ordered as following: $K_{\text{id},1} > K_{\text{id},2}$, implying the first stage refers to quick sorption on the most accessible active sites on the surface of the Cys nanocomposite (carboxylate, hydroxyl, and amine groups). After that, the concentration gradient between the solution and the sorbent diminished, slowing the mass transfer of uranyl ions to interior reactive groups (the structured material first interior layers and/or larger pores). Finally, the $K_{\text{id},3}$ -values were almost nil, as a result of the sorption-desorption equilibrium; it was assumed that sorption occurred in the micropores (the sorbent was nearing saturation) [35,37]. This implies that sorption via very tiny pores is governed by the resistance to intraparticle diffusion [38], as evidenced by a textural analysis.

Table 2. Uptake kinetics for UO_2^{2+} -parameters for the PFORE, PSORE, and sRIDE Model.

Model	Parameters	Values
$q_{\text{max, Exp.}}$	(mmol U/g)	0.455
PFORE	$K_1 \times 10^{-4} (\text{min}^{-1})$	748.478
	$q_{\text{max, cal.}}^*$	0.362
	R^2	0.953
PSORE	$K_2 \times 10^{-4} (\text{g}/\text{mmol} \cdot \text{min})$	550.230
	$q_{\text{max, cal.}}^*$	0.475
	R^2	0.998
sRIPD	$K_{\text{id},1}^{**}$	0.1051
	$K_{\text{id},2}$	0.0361
	$K_{\text{id},3}$	0.0009

* Units: (mmol U/g), and ** $K_{\text{id},x}$: $\text{mmol}/\text{g} \cdot \text{min}^{0.5}$.

The PFORE and PSORE were used to model the kinetic behavior (Table S1 for model equations). Heterogeneous reactions are described using the PFORE and PSORE models suggested and constructed for homogeneous chemical processes, under the assumption that apparent rate coefficients are implicitly functions of diffusion resistance [34]. Figure S3 shows the fitting of the experimental data and the parameters listed in Table 2. The PSORE's experimental data ($R^2 > 0.99$) had a substantially higher correlation coefficient

than the PFORE's ($R^2 \sim 0.95$). These findings show that the PSORE is an excellent model for understanding uranyl sorption, particularly chemisorption, which involves ion exchange and chelation mechanisms. Furthermore, the PSORE model fitness was validated by virtually the same sorption capabilities (calculated and experimental, Table 2): the PSORE data were overstated by $\sim 4.43\%$, whereas the PFORE data were underestimated by $\sim 20\%$. Moreover, the half-sorption time ($t_{0.5}$: the time it takes for the ion exchange resins to attain half of their maximal sorption capacity) was also calculated based on the acquired k_2 values. As mentioned ($t_{0.5} = 1/k_2 \cdot q_2$), the $t_{0.5}$ was able to be used to calculate the sorption rate, which was 3.83 min.

3.3.4. Sorption Isotherms

The sorption isotherms ($q_{eq} = f(C_{eq})$) show how the solute is distributed between the liquid (C_{eq}) and solid (q_{eq}) phases (for various initial concentrations (C_0), but for the same temperature and pH) [4,39]. Figure 5d depicts data on UO_2^{2+} sorption isotherms at pH_0 : 4.0 and various temperatures (298–328 K). The isotherm was characterized by a gradual increase in sorption capacity, followed by sorbent saturation at the maximum experimental sorption capacity of ~ 0.55 mmol U/g. The plateau revealed that the sorbent's most active sites reacted with UO_2^{2+} . Furthermore, the underlying curves at various temperatures show that temperature has a detrimental influence on sorption efficiency (i.e., exothermic feature).

Sorption isotherms can be modeled using Langmuir, Temkin, and Freundlich equations (Table S1 for model equations) [37,40,41]. Table 3 shows the computed parameters. The comparison of determination coefficients (R^2) for the Langmuir equation generally gives slightly higher coefficients ($R^2 > 0.99$) compared to the Freundlich ($R^2 < 0.91$) (Figure S4). Furthermore, the sorption capabilities matched the experimental data, and both the Langmuir and Freundlich models were persistently overstated (Δq_{eq} : 4.6–6.7%). As a result, Monolayer uniform sorption occurred, with a finite number of identical sites scattered over the sorbent surface. Moreover, the Langmuir constant (b_L) was proportional to the sorption energy; the higher the b_L value, the higher the sorption energy, and the greater the sorbent–sorbate affinity [40]. Table 3 illustrates that both the q_{max} and the b_L values slightly decreased with increasing temperature, and that the sorption was likely to have been slightly exothermic. The b_L values decreased (from 17.58 to 14.48) with increases in the temperature (from 298 K to 328 K). This means that at room temperature, sorption is more favorable.

Table 3. Sorption isotherms for UO_2^{2+} —the Langmuir, Freundlich, and Temkin equations all include model parameters.

T (K)	$q_{max.exp.}^*$	Langmuir Isotherm			Freundlich Isotherm			Temkin Isotherm		
		$q_{max.cal.}^*$	b_L (L/mmol)	R^2	$1/n$	K_F^*	R^2	A_T (L.mmol)	B_T (J/mol)	R^2
298	0.546	0.576	17.58	0.9996	0.1963	0.576	0.933	876.731	0.0831	0.970
308	0.522	0.553	16.49	0.9993	0.1987	0.549	0.914	789.342	0.0806	0.956
318	0.501	0.532	15.25	0.9993	0.2051	0.526	0.905	640.533	0.0796	0.949
328	0.480	0.512	14.48	0.9991	0.2052	0.502	0.9264	601.364	0.0769	0.964

* Units: (mmol U/g).

Figure S5 compares UO_2^{2+} sorption isotherms at pH_0 4.0 and C_0 : 1.25 mmol U/g at 298 K for CMCT and Cys: the maximal sorption capacities follow the following order: Cys (~ 0.546 mmol U/g) > CMCT (~ 0.291 mmol U/g). This indicates that the chemical functionalization significantly improved the sorption performance by about 1.88 times. This result supports and in agree with the findings of the pH factor.

Another model is the Temkin isotherm, which supposes that sorption free energy is proportional to surface coverage [35,41]. The Temkin model constants are reported in Table 3 and Figure S4. The constant A_T represents the sorbent's initial sorption heat: the higher the A_T , the greater the sorption heat, and the higher the sorbent's affinity for the

sorbate [41,42]. The A_T values reduced from 876.73 to 601.36 L/mmol, and the energetic parameter (A_T) decreased (from 0.0831 to 0.0769 J/mol) with increases in the temperature from 298 to 328 K, as previously observed (such as in the comparison of b_L and q_m in the Langmuir model) [42].

Based on the Langmuir isotherms (i.e., the b_L constant was employed after conversion (L mg⁻¹ to L mol⁻¹) and dimensionless processing (correcting with the water molality), according to Lima et al. [43]), the thermodynamics can be examined. Thermodynamic parameters are calculated by the Van't Hoff equation (Equations (12) and (13)) [35,41].

$$\ln b_L = -\frac{\Delta H^\circ}{R} \times \frac{1}{T} + \frac{\Delta S^\circ}{R} \quad (12)$$

$$\Delta G^\circ = \Delta H^\circ - T\Delta S^\circ \quad (13)$$

where the universal gas constant is R (8.314 J/mol.K), T (K) indicates absolute temperature, and b_L is the Langmuir constant. The ΔH° , and ΔS° values were obtained from the slope and intercept of the plot of $\ln b_L$ vs. $1/T$ (Figure 5d).

Table 4 summarizes the thermodynamic parameters. The exothermic nature was confirmed by ΔH° 's negative sign, and the reaction was more favorable at lower temperatures, as the ΔH° values were less than 40 kJ/mol, suggesting that physical forces were present in the UO_2^{2+} sorption process. The positive ΔS° value showed that the interaction between UO_2^{2+} and Cys would enhance entropy, resulting in more degrees of freedom for solute molecules [33]. The negative ΔG° values (in the same range from -35.18 to -37.61 kJ/mol) imply that the sorption process is spontaneous. The absolute ΔG° values were proportional with the temperature. Moreover, Table 5 indicates that the reaction was more controlled by entropic changes than by enthalpy changes ($|\Delta H^\circ| < |T\Delta S^\circ|$) (with values very close).

Table 4. Thermodynamic parameters for UO_2^{2+} sorption.

Temp. (K)	ΔH° (kJ/mol)	ΔS° (J/mol)	ΔG° (kJ/mol)	$T\Delta S^\circ$ (kJ/mol)	R^2
298	−6.131	97.473	−35.18	29.05	0.9872
308			−36.15	30.02	
318			−37.13	31.00	
323			−37.61	31.48	

Table 5. Uranium sorption performances using different sorbents.

Sorbent	pH ₀	T _{eq} (min)	SD (g/L)	Temp. (K)	q _{m,exp} *	q _{m,L} *	b _L (L/mmol)	Ref.
HCPs	8.0	70	1.0	308	0.196	0.200	14.520	[33]
SIL	4.0	60	1.0	325	0.168	0.157	19.753	[44]
Arg-Cell Glu-Cell	5.0	180	0.5	318	0.581 0.676	0.618 0.705	17.852 24.993	[12]
CA CA-PO ₄	5.5	120	1.0	298	0.431 0.631	0.431 0.631	26.183 52.366	[45]
DETA-MC	4.0	60	0.2	298	0.748	0.778	22.137	[5]
HA-MCNPs	5–7	20	1.0	333	46.3	47.9	3.166	[46]
Mag. Schiff base	6.0	360	0.02	298	0.396	0.416	138.176	[47]
Schiff's base-MC	4.0	20	1.0	298	2.322	2.454	1.800	[48]
HTC-Acy	4.5	120	1.0	335	1.716	—	—	[49]
Cys	4.0	50	0.5	298	0.547	0.576	17.58	Here

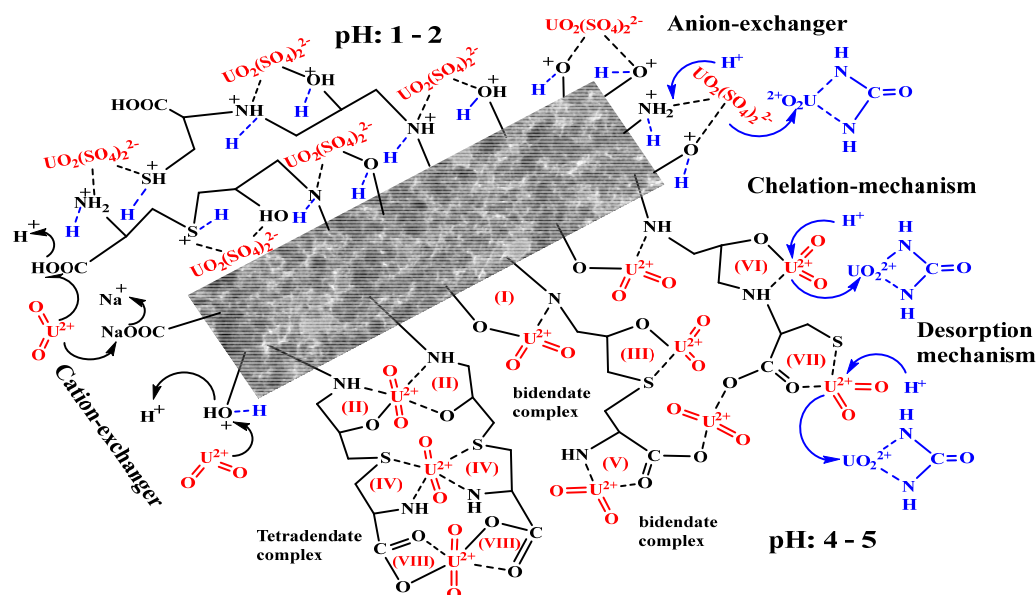
* Unit: mmol U/g.

3.3.5. Comparison of Sorbent Properties for Different Sorbent Material

Compared with other sorption materials, the Cys nanocomposite had an excellent sorption performance, although a direct comparison was difficult due to the differences in experimental settings (Table 5). The nanocomposite sorbent had a good maximum sorption capacity, its equilibrium time was found to be 50 min, and it had a wide range of pH: 3.5–5.0, which indicates that sorbent is the appropriate candidate for uranium sorption.

3.3.6. Metal Desorption and Recycling

To improve the cost effectiveness, the uranium concentration for final recovery should be improved, and the sorbent should be regenerated and recyclable. Metal desorption from a variety of functionalized resins was particularly efficient with NaHCO_3 and acidic urea solutions [5,34]. Sorption/desorption were performed repeatedly using acidified urea (0.25 M at pH 2.5) by H_2SO_4 as an eluent, and the proposed desorption mechanism was depicted in Scheme 2. Table 6 reports six successive sorption/desorption cycles: both the sorption and desorption efficiencies fell somewhat for each sorption step. At the end of the sixth cycle, the sorption and desorption processes had efficiency losses of less than 9% and 5%, respectively. In terms of sorption capacity, this suggested that the sorbent had strong durability, reusability, and stability.



Scheme 2. Tentative U^{VI} (UO_2^{2+} and $\text{UO}_2(\text{SO}_4)_2^{2-}$) sorption interactions modes between reactive groups and desorption from metal-loaded sorbent.

Table 6. Metal desorption and sorbent recycling.

Cycle No.	Sorption Step			Desorption Step		
	SE (%)	St. Dev.	qeq (mmol U/g)	DE (%)	St. Dev.	Eluate Conc. (mmol U/L)
	Average		Average	Average		Average
1	100 *	0.00	0.515	97.88	0.19	0.504
2	97.11	0.08	0.500	96.77	0.26	0.498
3	95.65	0.17	0.492	95.05	0.48	0.480
4	93.81	0.06	0.483	95.43	0.86	0.476
5	92.36	0.25	0.475	94.07	0.50	0.454
6	91.52	0.05	0.471	93.00	0.76	0.442
$\Delta(1\text{st}/6\text{th})$	-8.48			-4.88		

Sorption efficiency (SE) and desorption efficiency (DE). * Standard metal ion sorption efficiency (at first cycle).

3.3.7. Uranyl Species Interactions and Mechanisms

The numerous functional groups involved in the uranium sorption process were predicted using extensive spectroscopic analyses (FTIR and XPS).

FTIR Spectroscopy

FTIR spectra were used for characterizing the interaction modes and, more specifically, for identifying the reactive groups affected by the binding of UO_2^{2+} (Figure 3). Basically, the two spectra were almost identical; the significant differences were observed in the form of minor band shifts and decreased peak intensities and broadness in the transmittance spectra when compared, but also in the form of the disappearance of typical bands.

(a) The most notable changes were detected at around 3402 cm^{-1} ; the broad band (overlapped bands for $-\text{OH}$ and $-\text{NH}$ stretching vibrations) was little shifted and its width and intensity decreased, as a result of its role in metal ion chelation and sorption.

(b) The bands' intensity tended to strongly decrease and red-shift at 2916 cm^{-1} and 2873 cm^{-1} (assigned to $-\text{CH}_2$ groups), moving to 2917 cm^{-1} and 2871 cm^{-1} , respectively. These alterations and changes are directly related to metal ion binding, which changes the $-\text{OH}$ and $-\text{NH}$ groups' surroundings (band superimpositions that are not well-resolved).

(c) The intensity of bands tended to decrease and red-shift at 1628 cm^{-1} to 1631 cm^{-1} , which was probably due to the contribution of amine and carboxylate groups, demonstrating a preference for active sites with O- and N-atoms.

(d) The bands at 1385 cm^{-1} and 1066 cm^{-1} (attributable to N-H vibrations in secondary amines and primary/secondary $-\text{OH}$ stretching, respectively) moved to 1382 cm^{-1} and 1061 cm^{-1} ; these changes were associated with $\text{UO}_2^{2+}-\text{N}$ and $\text{UO}_2^{2+}-\text{O}$ bonds of N-H and O-H vibrations.

(e) The peak vanished at 742 cm^{-1} (weaker C-S bond stretching vibration), indicating that C-S reactive groups are significant in UO_2^{2+} binding.

(f) The other significant change (band width and intensity), which was observed at $600\text{--}1100\text{ cm}^{-1}$, was affected by metal sorption.

(g) Finally, the absence of characteristic peaks of the linear vibration of UO_2^{2+} at 823 cm^{-1} and 913 cm^{-1} [34] could not be observed due to it overlapping with other active sites and/or the UO_2^{2+} contents being too small. However, the XPS analysis verified this.

The desorption spectrum (at the end of the sixth desorption cycle) partly recovered the sorbent, which was exceptionally stable. However, it is noteworthy that many tracer bands of metal sorption remained on the FTIR spectra of the regenerated sorbent, and/or were associated with the effects of environmental conditions (such as pH effect (pH_0 : 4.0)), which can be considered as "intermediary" spectra between raw and metal-loaded sorbents. As seen at the 3402 cm^{-1} , $2916\text{--}2873\text{ cm}^{-1}$, 1628 cm^{-1} , 1385 cm^{-1} , $1066\text{--}1032\text{ cm}^{-1}$, and $750\text{--}400\text{ cm}^{-1}$ regions, the spectrum still had not been fully restored.

XPS Spectroscopy

Figure S1 shows the core level spectra for key elements. The deconvoluted bands, via the assignments and relative atomic fractions for the C 1s, O 2s, N 1s, S 2p, Fe 2p, and U 4f signals from HRES spectra for the Cys nanocomposite before and after uranium complexation, are summarized in Table 7. The observed variations in the relative contributions of the different bands and the shift in BEs were mainly followed by $\text{U}^{(\text{VI})}$ interaction with N-containing groups (amine), S-containing groups (thiolate/ $-\text{SH}$), and O-containing groups ($-\text{OH}/-\text{COO}^-$), as indications of reactive groups' participation in metal ion binding and/or reactive group chemical alterations.

Table 7. Assignment of the core-level signals: Binding energies (BEs) and atomic fraction (AF, %).

Signal	Bef. U-Sorption		Aft. U-Sorption		Possible Chemical Assignments
	BE (eV)	AF (%)	BE (eV)	AF (%)	
C 1s	285.36	22.88	285.84	35.89	C–H, C–C
	286.37	24.32	286.5	46.5	C–S, C–N, C–O, C–O–C,
	287.23	52.8	288.24	17.57	C=O, COO [−]
O 1s	530.17	20.29	530.4	20.85	Lattice O (Fe–O, Fe ₃ O ₄)
	531.99	42.76	532.53	59.27	C=O, O–C=O
	532.98	36.95	533.14	19.88	C–OH, H ₂ O, C–O–C, Metal(OH) _x
N 1s	399.54	64.37	399.41	30.59	C–N
	401.36	35.63	400.9	69.41	–NH ₂ , >NH
S 2p	164.17	82.27	164.17	59.11	C–S (2p _{3/2})
	168.05	17.73	167.98	14.43	C–S–C (S 2p _{1/2})
			169.43	26.47	S–O (S 2p _{3/2} Sulfate)
Fe 2p	710.68	31.18	710.92	42.75	Fe 2p _{3/2} (Fe ³⁺ –octa)
	713.23	19.42	713.45	16.2	Fe 2p _{3/2} (multipl–Fe ²⁺ –octa)
	716.96	7.97	717.02	5.62	Fe 2p _{3/2} (Fe ³⁺ –tetra)
	719.99	8.72	720.02	4.25	Fe 2p _{1/2} (Fe ³⁺ –Satallite)
	724.31	19.88	724.1	17.36	Fe 2p _{1/2} (Fe ²⁺ –octa)
	727.69	7.8	726.91	9.48	Fe 2p _{1/2} (Fe ³⁺ –tetra)
	732.39	4.97	733.21	4.34	Fe 2p _{3/2} (Fe ³⁺ –octa)
U 4f			381.82	58.44	U 4f _{7/2} (U ^(VI))
			385.61	6.12	U 4f _{7/2} (U ^(VI) –Satellite)
			392.12	22	U 4f _{5/2} (U ^(VI))
			393.07	13.44	U 4f _{5/2} (U ^(VI) –Satellite)

(a) C 1s signal intensities were significantly affected after U^(VI) sorption; individual component peaks were identified at 285.36 eV (C–C and C–O), 286.37 eV (corresponding to C–S/C–SH, C–NH and C–OH), and 287.23 eV (C=O and –COO[−]) [50].

(b) The O 1s signal showed strong changes after U(VI) sorption; the increase in the band intensity at 531.99 eV corresponding to the C=O and O–C=O function was involved in metal sorption, while decreases at 532.92 eV (C–OH/C–O–C of carbohydrate ring and interchain bonding) occurred due to the environment of these reactive groups [50]. With the inclusion of magnetite (Lattice O signal for magnetite Fe–O), a band at 530.7 eV (of constant intensity) developed

(c) N 1s appeared after cysteine grafting; the band's relative intensity at 400.9 eV (–NH₂, >NH) was increased with a shift in BE to 400.90 eV (where secondary amine (>NH) from chitosan moiety and primary amine (–NH₂) from cysteine moiety were involved in uranium sorption). Meanwhile, that of C–N and N–H, as well as N–U (399.5 eV), decreased.

(d) The S 2p signal confirmed the occurrence of S-atom in the Cys sorbent as an organic form. The asymmetric S 2p peak was deconvoluted into two subpeaks assigned to S 2p_{3/2} and S 2p_{1/2}, which were noticed at 164.17 eV and 168.05 eV, respectively, indicating the S^{2−} presence as C–S–C [51]. There was a relative decrease in their intensity, indicating that S-atom is involved in U sorption as a chelation thiolate–U via S-orbitals. Hamza et al. [52] reported that metal ion sorption is mainly followed by: (a) changes in the relative contributions of the various bonds, and (b) shifts in BEs, as tracers of the involvement of reactive groups in the binding of metal anions, and/or the chemical modifications of reactive groups (associated with the reduction of U(VI) and the oxidation of the surface groups on the sorbent). Surprisingly, a new peak arose at 169.43 eV after U^(VI) sorption, confirming the existence of inorganic sulphate anions (SO₄^{2−}) immediately on an ion pair (protonated amine groups) at the sorbent's surface. This was likely owing to the sorption of uranyl sulfate forms (speciation of uranyl anions from sulfate medium), confirming that anion-exchange mechanisms were involved (See Scheme 2 below).

(e) The Fe 2*p* signal showed the primary peaks of Fe³⁺ 2*p*_{3/2} and Fe³⁺ 2*p*_{1/2}, which were regarded to be unique Fe₃O₄ spectra, and these were situated at 711.18 and 724.31 eV, respectively [53,54]. By fitting the Fe 2*p* double peak, the Fe 2*p*_{3/2} peaks emerged at 710.68 and 713.23 eV, and the Fe 2*p*_{1/2} peaks appeared at 719.99 and 724.31 eV, respectively, confirming the existence of Fe²⁺ and Fe³⁺, respectively, corresponding to Fe₃O₄ [54]. A Fe 2*p*_{3/2} satellite and Fe 2*p*_{1/2} satellite appeared at 718.2, and 732.39 eV, respectively [54,55]. However, Fe₃O₄ nanoparticles and Fe²⁺ shakeup satellite peaks (at 716.96 eV) can be observed beside the Fe³⁺ shakeup satellite (at 719.99 eV) due to Fe atoms migrating to the surface and the ease of identification by XPS [54,55]. After sorption, no impressive changes were observed (Figure S1: Fe 2*p* signal), because Fe atoms are at the structure's core and the sorption of UO₂²⁺ has no affect them [54].

(f) For U 4*f* excitations, deconvoluting core level spectra into two main spin-orbits (L-S) split the U 4*f*_{7/2} and U 4*f*_{5/2} signals at about ~381.65 and ~392.26 eV, respectively, consistent with previously reported spectra [30,31]. Inspection of the satellite peaks showed the occurrence of peaks at 4 and 7 eV from the U 4*f*_{7/2}. Shake-up satellites are low-intensity excitations that arise as a result of the photoelectron excitation process's shift in electrostatic potential [30]. The core level electron kinetic energy will drop as a result, and an additional/satellite peak will form on the high binding energy (BE) side of the main peak [30,31].

3.3.8. Metal Interaction Mechanism

Based on the effect of pH results, FTIR and XPS data show that distinct strategies were used in uranium sorption (Scheme 2):

- Anion-exchange mechanism of anionic UO₂(SO₄)₂²⁻ species via SO₄²⁻ on the protonated amine groups;
- Cation-exchange mechanism with cationic species (UO₂²⁺) at higher pH₀, but less than pH_{PZC} (i.e., can deprotonate active sites), with the Na⁺ attached to -COO⁻ and H⁺ of the -OH and -NH₂/ $>$ NH groups;
- Chelation and complexation mechanisms of UO₂²⁺, with different heteroatoms (O and N) on the surface of the sorbent.

The chelation and complexation interaction mechanism of U^(VI) with Cys, via various O-, S-, and N-atoms, produced metal-ligand interactions. This was clarified with XPS findings at the molecular level by comparing the raw Cys before and after U^(VI) loading. The high-resolution C 1*s* spectra (Figure S1) suggest some differences between the C 1*s* peak for the raw Cys before and after sorption of U^(VI). Significant differences (both in intensities and peak positions) can be observed for the S 2*p*, N 1*s*, and O 2*s* signals, which are associated with sulfur-, nitrogen-, and oxygen-containing functional groups, such as the -S- in the thiolate linker, the -SH thiolate group (via amine linked with cysteine), $>$ NH in the chitosan molecule, terminal -NH₂ bonds in the cysteine group, $>$ C=O, -COO⁻ of the cysteine moiety, and -OH in the chitosan molecule in a single sorbent chain.

A putative mechanism for the uranyl metal ion complex may be hypothesized based on XPS and FTIR investigations (Scheme 2). Metal ions were bound via the following mechanisms: (a) two coordinating bonds with the N-atom of $>$ NH group, the O-atom of primary C4-OH in the chitosan molecule itself (the contribution modes I), and with the secondary (-OH) from the epichlorohydrin binder between chitosan and the cysteine moiety (the contribution modes II); (b) two coordination bonds with the O-atom of secondary (-OH) from the epichlorohydrin binder primary hydroxyl group, and the S-atom in the thiolate linker of the cysteine moiety (the contribution modes III); (c) two coordination bonds with S-atom of the thiolate linker and the N-atom of the amine group in the cysteine moiety (the contribution modes IV); (d) two coordination bonds with the O-atom of ($>$ C=O) carbonyl group, the N-atom of the amine group in the cysteine moiety (the contribution modes V); and, finally, (e) two coordination bonds with oxygen atoms of the carboxylate group, forming four membered rings. Another mode of cysteine-linking to the matrix via amine group was observed, as explained above (Section 3.1), so it had a free terminal thiol-group

(–SH) that could give contribution modes VI and VII). Thus, contribution modes I to VI and VII formed stable five- and six-membered chelating rings, respectively, whereas modes VIII formed an unstable four-membered ring. Moreover, another interaction mode between UO_2^{2+} and active sites from two chains formed two chelating rings (with five members in size). By increasing the number of chelate rings, the formed complex's stability improved, and the metal sorption capacity improved as a result (Scheme 2).

Moreover, the anion-exchange mechanism of uranium sorption by amine groups [56], and the suspected anion-exchange reactions were poorly probable: The overall ion-exchange reaction (Equations (14) and (15)):



Another ion-exchange mechanism for the neutral uranium sulfate species:



Finally, it is noteworthy that the proposed desorption process, depicted in Scheme 2, used acidified urea in the desorption stage, as the acidity of this solution can facilitate and break the contribution modes; in addition, urea can coordinate and bond with two N-donors of $-\text{NH}_2$ in the urea $\text{CO}(\text{NH}_2)_2$ molecule; this confirms the expected mechanism.

3.3.9. Tests of Selectivity

The selectivity sorption of UO_2^{2+} from a simulated nuclear industrial effluent (in multi-component equimolar solutions) was examined. In terms of sorption capacities (q_{eq} , mmol/g), the distribution ratio (D , L/g), and the selectivity coefficient ($\text{SC}_{\text{metal}/\text{U}} = D_{\text{metal}}/D_{\text{U}}$) [4], the data were analyzed (Figure 6). The uranium sorption capacity reached 0.354 mmol U/g, which was significantly lower than that of synthetic solutions (0.546 mmol U/g). This suggests that excessive concentrations of co-ions lower maximum sorption by 35.17%; considering the significant abundance of coexisting ions, the sorbent has a strong preference for UO_2^{2+} . Despite the solution complexity, potential changes in metal speciation (due to nitrate anion) and the possible competitive impact of other metal ions should be noted. Other co-metal ions attached to the particular reactive sites through various stoichiometric ratios and/or distinct functional groups, resulting in a total sorption capacity of 0.580 mmol metal/g greater than that of UO_2^{2+} in synthetic solutions. The distribution ratio (D : q_e/C_e) and the selectivity coefficients ($\text{SC}_{\text{metal}/\text{U}}$) were calculated, which highlighted more efficiently the selectivity for the target metal. Hence, $\text{U}^{(\text{VI})}$ had higher D values (1.08 L/g) and $\text{SC}_{\text{metal}/\text{U}}$ values than other co-ions; the sorbent, thus, has preferential affinity and competitiveness for highly selective uranium sorption.

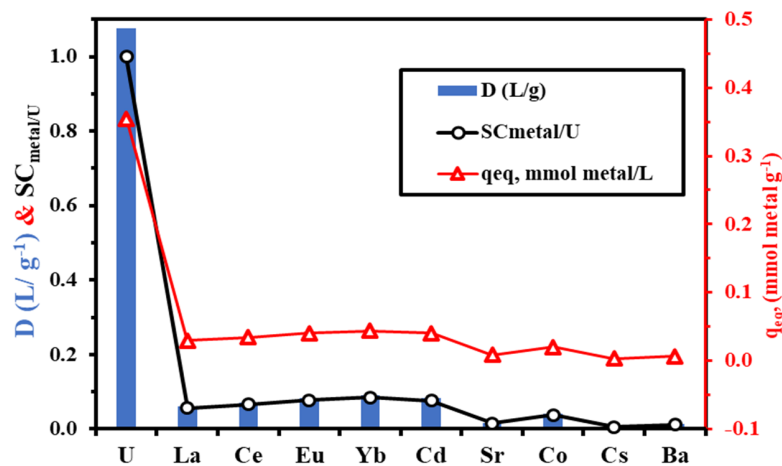


Figure 6. Sorption capacities, distribution coefficients, and selectivity coefficient ($\text{SC}_{\text{metal}/\text{U}}$) in selectivity tests (SD: 0.5 g/L, C_0 : 0.5 mmol/L, pH_0 : 4.0, T: 298 ± 1 K, Time: 180 min, 200 rpm).

Figure 7 depicts the relative molar percentages of various co-metal ions in the initial tested pregnant liquor, treated liquor raffinate, and the metal ions adsorbed onto the surface of Cys sorbent. There was a significant difference in the solution before and after sorption. The residue concentration of uranium after the sorption process was about 7% molar percent and the sorbent. This is the first proof that the selectivity is quite high for uranium. In comparison to the leachate's original composition, the percentages in the sorbent reflect a wide range of trends: UO_2^{2+} exhibited a significant enrichment and concentration (from 10.0% to 61%), as well as to a lesser extent for ΣREEs ' 149.4 $\mu\text{mol RE/g}$; 85.1 $\mu\text{mol HREs/g}$ represented ~58% of the total capacity (i.e., 44.9 and 40.1 $\mu\text{mol/g}$ for $\text{Yb}^{(\text{III})}$ and $\text{Eu}^{(\text{III})}$, respectively), and 64.4 $\mu\text{mol LREs/g}$ represented ~42% of the total capacity (i.e., 34.5 and 29.9 $\mu\text{mol/g}$ for $\text{Ce}^{(\text{III})}$ and $\text{La}^{(\text{III})}$, respectively). Alternatively, the sorption capacity of other metal ions represented ~13.5% of the total sorption capacity of ≈ 78.1 $\mu\text{mol/g}$, including 40.4 $\mu\text{mol/g}$ of $\text{Cd}^{(\text{II})}$, which represented about 51.8% of the total other metal ions, and about 7% of the total sorbent sorption capacity. The selectivity for $\text{Cd}^{(\text{II})}$ over other metal ions was likely related to the existence of functional groups that are S-bearing (soft base), which are more sensitive to soft acids such $\text{Cd}^{(\text{II})}$ [4], lowering the Cys sorbent overall selectivity for UO_2^{2+} . Moreover, the poor sorption efficiency for both Sr(II) and Cs(I) may be explained by the fact that they have a greater affinity for the ion-exchanger inorganic sorbents than the organic chelation sorbents [57]. Moreover, the QSAR (quantitative structure activity relationship) tools were applied for correlating the sorption properties and selectivity coefficients of the sorbent for the co-metal ions to their specific physicochemical characteristics (e.g., atomic number, electronegativity, and hydrated ionic radius), in order to explain the high selectivity of the uranium over other co-metal ions in the liquor.

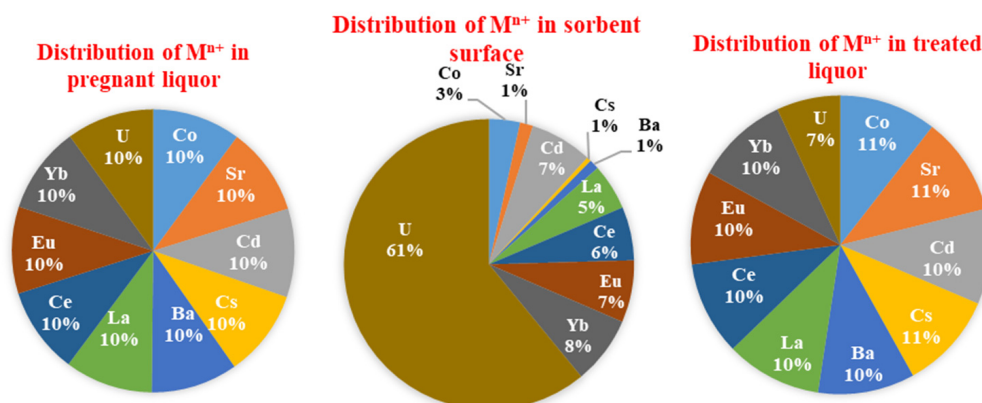


Figure 7. The distribution of the selected metal ions in pregnant liquor, treated liquor, and the Cys-sorbent (molar percentages).

Rashad et al. (2021) [42] stated that various factors may regulate the preference of uranyl ions for different sorbents:

- According to Pearson's principles (the HSAB concept), uranyl is a hard acid, which indicates that the metal ion binds preferentially to ligands containing $\text{O} \gg \text{N} \gg \text{S}$ [58];
- The electron-withdrawing/releasing effect affects the donating ability of the different functional groups (negatively for carboxylic acid groups, positively for amine groups);
- Uranium is present in oxycation form (UO_2^{2+}), which can be adsorbed in different forms with different mechanisms, as reported in our study;
- The steric effect modulates the stability and accessibility to reactive groups: herein, the contribution modes involved sulfur atoms, forming stable five- and six-membered chelating rings, while in other modes forming four membered rings (i.e., stronger steric hindrance when compared with five-/six-membered rings).

The relationships between the atomic number, the enrichment factor (EF = molar percentage ratio on the sorbent relative to that in the leachate [39]), and the distribution coefficient (D) are shown in Figure 8a,b. The figure reveals obvious trends: the enrichment factor for U(VI) exceeded 6, and raised as the atomic number increased; the same can be observed for the Cd(II), while heavy rare earth ions (HREs) were over light rare earths (with $EF > 0.5$), and the final other co-metal ions demonstrated a reciprocal tendency. Obviously, the linear curves clearly exclude uranium: U is commonly connected with REEs, due to its atomic number (92). However, the EF order of magnitude was the same as that of HREs. The distribution coefficients, which were much greater for HREEs than for LREEs when compared to other co-ions in the solution, showed the same results. This means that for the REs, both EF and D increased with increases in the atomic number, contrary to the behavior of the other metal ions (i.e., they followed a reciprocal trend). Comparing the chemical characteristics of selected metal ions in Table 8 reveals that the U element was extremely similar to RE elements in terms of ionic radii and electronegativity (Pauling units), but differed significantly in term of atomic mass. The U point shifted to its “equivalent atomic number” deviated significantly from the REs’ linear trends.

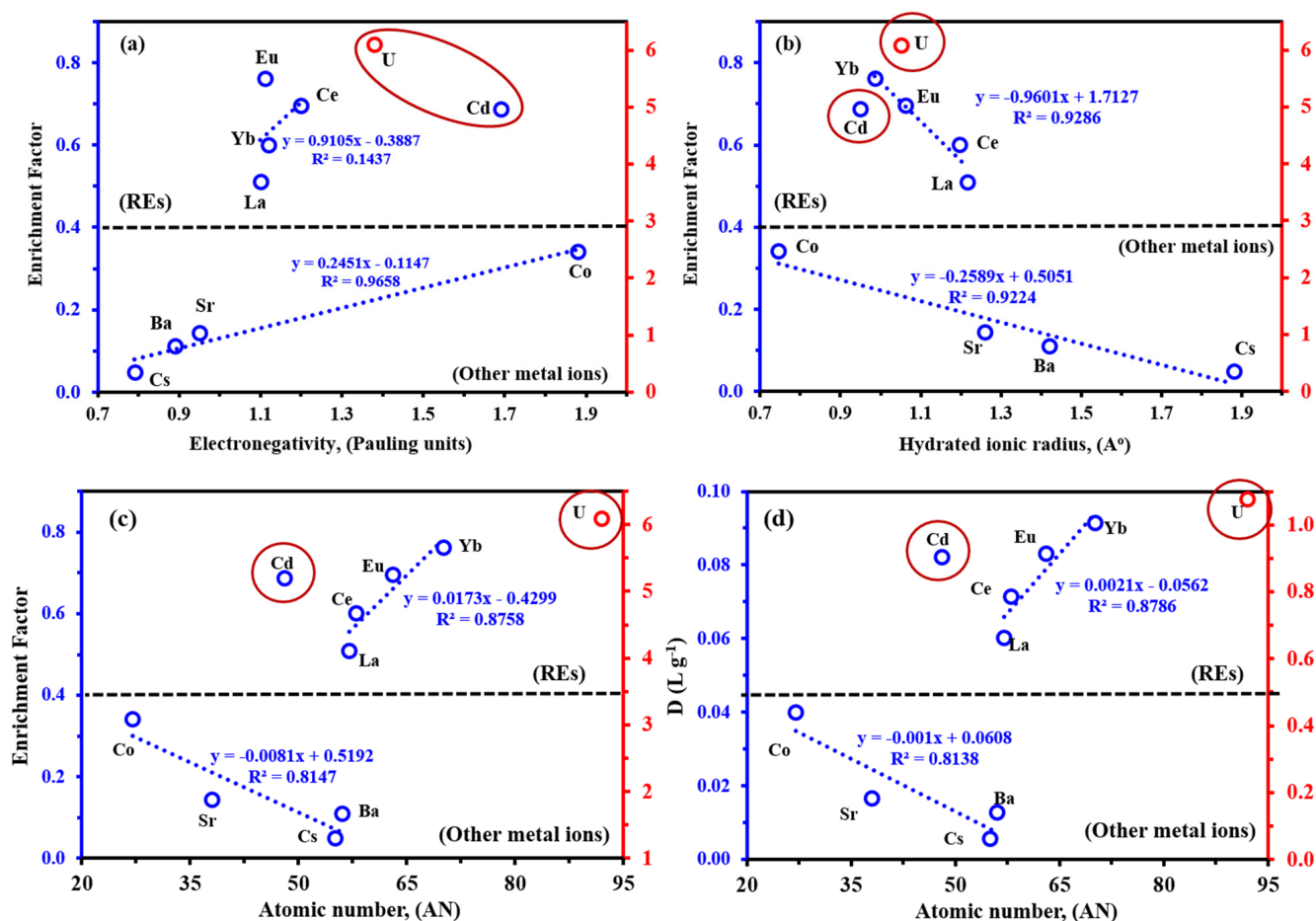


Figure 8. Correlation between atomic number and (a) enrichment factor and (b) distribution coefficient (D). Enrichment Factor and electronegativity (c) and hydrated ionic radius correlations (d).

Table 8. Chemical properties of some selected metal ions (under experiments).

Element	Atomic Number	Hydrated Species	M-O Bond Distance (Å)	M ⁿ⁺ Ion Radius (Å) [59]	M ⁿ⁺ Ion Radius, (Å) [58]	Electronegativity (Pauling Units)
Co	27	Co(H ₂ O) ₆ ²⁺	2.08	0.74	0.745	1.88
Sr	38	Sr(H ₂ O) ₈ ²⁺	2.62	1.28	1.26	0.95
Cd	48	Cd(H ₂ O) ₆ ²⁺	2.3	0.96	0.95	1.69
Cs	55	Cs(H ₂ O) ₁₂ ⁺	3.25 *	1.91 *	1.88	0.79
Ba	56	Ba(H ₂ O) ₈ ²⁺	2.82	1.48	1.42	0.89
La	57	La(H ₂ O) ₉ ³⁺	2.52 + 2.64	1.18 + 1.30	1.216	1.1
Ce	58	Ce(H ₂ O) ₉ ³⁺	2.54	1.2	1.196	1.12
Eu	63	Eu(H ₂ O) ₉ ³⁺	2.425	1.085	1.062	1.2
Yb	70	Yb(H ₂ O) _{8.5} ³⁺	2.32	0.98	0.985	1.11
U	92	U(H ₂ O) ₉ ⁴⁺	2.42	1.08	1.05	1.38
		UO ₂ (H ₂ O) ₅ ²⁺	(1.70) + 2.42	1.08		1.38

* Information based on solid-state structures.

Figure 8c,d depicts the relationship between the enrichment factor for REs and other co-metal ions' electronegativity and hydrated ionic radii. Generally, the hydrated ionic radius was inversely proportional with the enrichment factor after the exclusion of border elements (U and Cd), with little or no enrichment factor change observed. For REs (Yb, Eu, Ce, and La elements), the electronegativity had an irregular/did not contribute on the enrichment factor. Meanwhile, the ER of other metal ions improved and raised with electronegativity, and reduced as the hydration ionic radius increased.

4. Conclusions

In this study, a hybrid mesoporous magnetic chitosan nanocomposite was successfully functionalized by cysteine to prepare a Cys sorbent for the sorption of uranyl ions selectively and efficiently from aqueous solution and radioactive effluents. A wide variety of analytical methods (including the CHNS, XRD, BET, pHpzc, TEM, XPS, FTIR, and VSM analyses) were used to determine the nanocomposites' physicochemical characteristics. The TEM micrograph determined the actual size of Fe₃O₄-nanocomposite and the morphology as well. The Fe₃O₄ NPs average particle size was found to be 14.01 ± 3.7 nm with a narrow size distribution, according to the obtained histogram with a regular spherical dot structure. The mesoporous sorbent had large surface-to-volume ratios (~42.56 m²/g and 0.11 cm³/g, respectively), and a unipore structure (~3.6 nm). Batch experimental studies showed that the sorption equilibrated within 50 min, sorbent dose 0.5 g/L, and the sorption capacity was ~0.575 mmol U/g, at 298 K, over a wide range of pH₀: (3.5–5.0). The sorption complied with pseudo-second-order and Langmuir models, implying that the sorption process tended to be a monolayer chemical sorption process. The comprehensive investigation (FTIR and XPS analysis) of surface interaction speculation found that thiolate, amino, and hydroxyl functional groups were identified as the main reactive groups that absorbed UO₂²⁺ on the surface of sorbents through ion exchange, electrostatic attraction, and chelation mechanisms. Thermodynamic parameters illustrated that the reaction exhibited spontaneous and exothermic behavior. An acidic urea solution (0.25 M, pH₀: 2.5) can be used to elute uranyl ions from metal-loaded sorbent. After six successive sorption/desorption cycles: the efficiency of the sorption and desorption processes were less than 9% and 5%, respectively. Competitive sorption–desorption experiments for UO₂²⁺ showed that the sorbent had considerably efficient sorption, durability, and reusability. U^(VI) showed higher selectivity coefficient and distribution ratio values (1.08 L/g) than other co-metal ions, indicating that the sorbent was efficient in the selective recovery of the uranium from simulated nuclear waste solution. The superparamagnetic properties of the nanocomposites (*M*_s: ~25.80 emu/g) indicate that the sorbent has broad prospects for use in removing uranium from solution.

Supplementary Materials: The following supporting information can be downloaded at: <https://www.mdpi.com/article/10.3390/polym14132568/s1>, Table S1. Sorption modeling: kinetics and sorption isotherms. Figure S1. XPS core level spectra for C 1s, O 1s, N 1s, P 2p, Fe 2p, and U 4f for Cys-sorbent before and after UO_2^{2+} sorption. Figure S2. Effect of sorbent dosage (a), Plot of pH_0 vs. pH_{eq} (b), $\log_{10}D$ plot vs. pH_{eq} (b), and plot of pH_0 vs. q_{eq} (c) for UO_2^{2+} sorption. Figure S3. Sorption kinetics for PFORE, PSORE, and Intraparticle diffusion. (C_0 : 0.425 mmol U/L, SD: 0.5g/L, time 60 min, room temp. 298 K), and Figure S4. Linearization plots of Langmuir (a), Freundlich (b), and Timken isotherm (c): for UO_2^{2+} sorption. (pH_0 : 4.0, SD: 0.5 g L⁻¹, C_0 : 0.21–1.26 mmol U/L; T: 298–328 K, Time: 60 min.). Figure S5. Sorption isotherm using both CMCT and Cys nanocomposites for UO_2^{2+} sorption. (pH_0 : 4.0, SD: 0.5 g/L, C_0 : 0.21–1.26 mmol U/L, T: 298–328 K, Time: 60 min for Cys and 180 min for CMCT).

Author Contributions: Conceptualization, A.A.A.-G., A.A.G. and S.W.; methodology, A.A.G. and S.W.; formal analysis, A.A.A.-G., Y.A.A.-T., A.A.G., A.M.A.-A. and A.A.; investigation, A.A.G., A.A.A.-G. and S.W.; resources, A.A.A.-G., Y.A.A.-T., A.A., A.M.A.-A. and A.A.G.; data curation, A.A.G. and S.W.; writing—original draft preparation, A.A.G.; writing—review and editing, A.A.A.-G. and S.W.; visualization, A.A.A.-G., A.A.G., A.A. and S.W.; supervision, A.A.A.-G. and S.W.; project administration, A.A.A.-G., S.W., Y.A.A.-T. and A.A.G.; funding acquisition, S.W. and A.A.A.-G. All authors have read and agreed to the published version of the manuscript.

Funding: This research was funded by Deputyship for Research & Innovation, Ministry of Education in Saudi Arabia, grant number (IFPNC-004-130-2020) and The APC was funded by Deputyship for Research & Innovation, Ministry of Education in Saudi Arabia project number (IFPNC-004-130-2020).

Data Availability Statement: All data generated or analyzed during this study are included in this article.

Acknowledgments: The authors extend their appreciation to the Deputyship for Research & Innovation, Ministry of Education in Saudi Arabia for funding this research work through the project number (IFPNC-004- 130-2020) and King Abdulaziz University, DSR, Jeddah, Saudi Arabia.

Conflicts of Interest: The authors declare no conflict of interest.

References

1. Hu, C.; Zhang, L.; Zhao, Z.-J.; Li, A.; Chang, X.; Gong, J. Water Splitting: Synergism of Geometric Construction and Electronic Regulation: 3D Se-(NiCo)S_x/(OH)_x Nanosheets for Highly Efficient Overall Water Splitting. *Adv. Mater.* **2018**, *30*, 1870085. [[CrossRef](#)]
2. Yuan, Y.; Meng, Q.; Faheem, M.; Yang, Y.; Li, Z.; Wang, Z.; Deng, D.; Sun, F.; He, H.; Huang, Y.; et al. A molecular coordination template strategy for designing selective porous aromatic framework materials for uranyl capture. *ACS Cent. Sci.* **2019**, *5*, 1432–1439. [[CrossRef](#)] [[PubMed](#)]
3. Kawamata, Y.; Hayashi, K.; Carlson, E.; Shaji, S.; Waldmann, D.; Simmons, B.J.; Edwards, J.T.; Zapf, C.W.; Saito, M.; Baran, P.S. Chemoselective electrosynthesis using rapid alternating polarity. *J. Am. Chem. Soc.* **2021**, *143*, 16580–16588. [[CrossRef](#)]
4. Morshedy, A.S.; Galhoum, A.A.; Abdel Aleem, A.A.H.; Shehab El-din, M.T.; Okaba, D.M.; Mostafa, M.S.; Mira, H.I.; Yang, Z.; El-Sayed, I.E.T. Functionalized aminophosphonate chitosan-magnetic nanocomposites for Cd(II) removal from aqueous solutions: Performance and mechanisms of sorption. *Appl. Surf. Sci.* **2021**, *561*, 150069. [[CrossRef](#)]
5. Galhoum, A.A.; Mahfouz, M.G.; Goma, N.M.; Vincent, T.; Guibal, E. Chemical modifications of chitosan nano-based magnetic particles for enhanced uranyl sorption. *Hydrometallurgy* **2017**, *168*, 127–134. [[CrossRef](#)]
6. Galhoum, A.A.; Mahfouz, M.G.; Goma, N.A.; Abdel Rehem, S.S.; Atia, A.A.; Vincent, T.; Guibal, E. Cysteine-functionalized chitosan magnetic nano-based particles for the recovery of uranium(VI): Uptake kinetics and sorption isotherms. *Sep. Sci. Technol.* **2015**, *50*, 2776–2789.
7. Benettayeb, A.; Morsli, A.; Elwakeel, K.Z.; Hamza, M.F.; Guibal, E. Recovery of heavy metal ions using magnetic glycine-modified chitosan: Application to aqueous solutions and tailing leachate. *Appl. Sci.* **2021**, *11*, 8377. [[CrossRef](#)]
8. Abd El-Magied, M.O.; Galhoum, A.A.; Atia, A.A.; Tolba, A.A.; Maize, M.S.; Vincent, T.; Guibal, E. Cellulose and chitosan derivatives for enhanced sorption of erbium(III). *Colloids Surf. A: Physicochem. Eng. Asp.* **2017**, *529*, 580–593. [[CrossRef](#)]
9. Faulconer, E.K.; von Reitzenstein, N.V.; Mazyck, D.W. Optimization of magnetic powdered activated carbon for aqueous Hg(II) removal and magnetic recovery. *J. Hazard. Mater.* **2012**, *199–200*, 9–14. [[CrossRef](#)]
10. Coates, J. Interpretation of infrared spectra, a practical approach. In *Encyclopedia of Analytical Chemistry*; John Wiley & Sons Ltd.: Chichester, UK, 2006.
11. Tan, J.; Xie, S.; Wang, G.; Yu, C.W.; Zeng, T.; Cai, P.; Huang, H. Fabrication and optimization of the thermo-sensitive hydrogel carboxymethyl cellulose/poly(N-isopropylacrylamide-co-acrylic acid) for U(VI) removal from aqueous solution. *Polymers* **2020**, *12*, 151. [[CrossRef](#)]

12. El-Bohy, M.N.; Abdel-Monem, Y.K.; Rabie, K.A.; Farag, N.M.; Mahfouz, M.G.; Galhoum, A.A.; Guibal, E. Grafting of arginine and glutamic acid onto cellulose for enhanced uranyl sorption. *Cellulose* **2017**, *24*, 1427–1443. [CrossRef]
13. Li, N.; Bai, R. Copper adsorption on chitosan–cellulose hydrogel beads: Behaviors and mechanisms. *Sep. Purif. Technol.* **2005**, *42*, 237–247. [CrossRef]
14. Williams, R. Pka Data Compiled by R. Williams. 2017; pp. 1–33. Available online: <https://organicchemistrydata.org/hansreich/resources/pka/> (accessed on 10 May 2022).
15. Marotta, A.; Luzzi, E.; Salzano de Luna, M.; Aprea, P.; Ambrogi, V.; Filippone, G. Chitosan/Zelite composite aerogels for a fast and effective removal of both anionic and cationic dyes from water. *Polymers* **2021**, *13*, 1691. [CrossRef] [PubMed]
16. Michailidou, G.; Koumentakou, I.; Liakos, E.V.; Lazaridou, M.; Lambropoulou, D.A.; Bikiaris, D.N.; Kyzas, G.Z. Adsorption of uranium, mercury, and rare earth elements from aqueous solutions onto magnetic chitosan adsorbents: A review. *Polymers* **2021**, *13*, 3137. [CrossRef]
17. Mubarak, M.F.; Ragab, A.H.; Hosny, R.; Ahmed, I.A.; Ahmed, H.A.; El-Bahy, S.M.; El Shahawy, A. Enhanced performance of chitosan via a novel quaternary magnetic nanocomposite chitosan/grafted halloysitenanotubes@Zn_γFe₃O₄ for uptake of Cr(III), Fe(III), and Mn(II) from wastewater. *Polymers* **2021**, *13*, 2714. [CrossRef]
18. Kong, H.; Song, J.; Jang, J. One-step fabrication of magnetic γ -Fe₂O₃/polyrhodanine nanoparticles using in situ chemical oxidation polymerization and their antibacterial properties. *Chem. Commun.* **2010**, *46*, 6735–6737. [CrossRef]
19. Wall, S.B.; Oh, J.Y.; Diers, A.R.; Landar, A. Oxidative modification of proteins: An emerging mechanism of cell signaling. *Front. Physiol.* **2012**, *3*, 369. [CrossRef]
20. Imam, E.A.; El-Tantawy El-Sayed, I.; Mahfouz, M.G.; Tolba, A.A.; Akashi, T.; Galhoum, A.A.; Guibal, E. Synthesis of α -aminophosphonate functionalized chitosan sorbents: Effect of methyl vs phenyl group on uranium sorption. *Chem. Eng. J.* **2018**, *352*, 1022–1034. [CrossRef]
21. Mahdavi, M.; Ahmad, M.B.; Haron, M.J.; Namvar, F.; Nadi, B.; Rahman, M.Z.; Amin, J. Synthesis, surface modification and characterisation of biocompatible magnetic iron oxide nanoparticles for biomedical applications. *Molecules* **2013**, *18*, 7533–7548. [CrossRef]
22. Yamaura, M.; Camilo, R.L.; Sampaio, L.C.; Macêdo, M.A.; Nakamura, M.; Toma, H.E. Preparation and characterization of (3-aminopropyl)triethoxysilane-coated magnetite nanoparticles. *J. Magn. Magn. Mater.* **2004**, *279*, 210–217. [CrossRef]
23. Marczenko, Z.; Ramsay, C.G.; Jurecki, M. *Spectrophotometric Determination of Elements*; Horwood, E., Ed.; Halsted Press: Chichester, UK; New York, NY, USA, 1976.
24. Winsett, J.; Moilanen, A.; Paudel, K.; Kamali, S.; Ding, K.; Cribb, W.; Seifu, D.; Neupane, S. Quantitative determination of magnetite and maghemite in iron oxide nanoparticles using Mössbauer spectroscopy. *Appl. Sci.* **2019**, *1*, 1636. [CrossRef]
25. Pourmortazavi, S.M.; Sahebi, H.; Zandavar, H.; Mirsadeghi, S. Fabrication of Fe₃O₄ nanoparticles coated by extracted shrimp peels chitosan as sustainable adsorbents for removal of chromium contaminates from wastewater: The design of experiment. *Compos. B. Eng.* **2019**, *175*, 107130. [CrossRef]
26. Stoia, M.; Istrate, R.; Păcurariu, C. Investigation of magnetite nanoparticles stability in air by thermal analysis and FTIR spectroscopy. *J. Therm. Anal. Calorim.* **2016**, *125*, 1185–1198. [CrossRef]
27. Salazar Camacho, C.; Villalobos, M.; Rivas-Sánchez, M.d.l.L.; Arenas-Alatorre, J.; Alcaraz-Cienfuegos, J.; Gutiérrez-Ruiz, M.E. Characterization and surface reactivity of natural and synthetic magnetites. *Chem. Geol.* **2013**, *347*, 233–245. [CrossRef]
28. Oh, S.Y.; Yoo, D.I.; Shin, Y.; Kim, H.C.; Kim, H.Y.; Chung, Y.S.; Park, W.H.; Youk, J.H. Crystalline structure analysis of cellulose treated with sodium hydroxide and carbon dioxide by means of X-ray diffraction and FTIR spectroscopy. *Carbohydr. Res.* **2005**, *340*, 2376–2391. [CrossRef]
29. Muthuselvi, C.; Pandiarajan, S.S.; Ravikumar, B.; Athimoolam, S.; Srinivasan, N.; Krishnakumar, R.V. FT-IR and FT-Raman spectroscopic analyzes of indeno quinoxaline derivative crystal. *Asian J. Appl. Sci.* **2018**, *11*, 83–91. [CrossRef]
30. Gouder, T.; Eloirdi, R.; Caciuffo, R. Direct observation of pure pentavalent uranium in U₂O₅ thin films by high resolution photoemission spectroscopy. *Sci. Rep.* **2018**, *8*, 8306. [CrossRef]
31. Huang, Z.; Li, Z.; Zheng, L.; Zhou, L.; Chai, Z.; Wang, X.; Shi, W. Interaction mechanism of uranium(VI) with three-dimensional graphene oxide-chitosan composite: Insights from batch experiments, IR, XPS, and EXAFS spectroscopy. *Chem. Eng. J.* **2017**, *328*, 1066–1074. [CrossRef]
32. Guo, J.; Yu, J. Sorption characteristics and mechanisms of Pb(II) from aqueous solution by using bioflocculant MBFR10543. *Appl. Microbiol. Biotechnol.* **2014**, *98*, 6431–6441. [CrossRef]
33. Bai, J.; Ma, X.; Yan, H.; Zhu, J.; Wang, K.; Wang, J. A novel functional porous organic polymer for the removal of uranium from wastewater. *Microporous Mesoporous Mater.* **2020**, *306*, 110441. [CrossRef]
34. Galhoum, A.A.; Eisa, W.H.; El-Tantawy El-Sayed, I.; Tolba, A.A.; Shalaby, Z.M.; Mohamady, S.I.; Muhammad, S.S.; Hussien, S.S.; Akashi, T.; Guibal, E. A new route for manufacturing poly(aminophosphonic)-functionalized poly(glycidyl methacrylate)-magnetic nanocomposite-application to uranium sorption from ore leachate. *Environ. Pollut.* **2020**, *264*, 114797. [CrossRef] [PubMed]
35. Tien, C. *Adsorption Calculations and Modeling*; Butterworth-Heinemann: Boston, MA, USA, 1994.
36. Hu, X.; Chen, C.; Zhang, D.; Xue, Y. Kinetics, isotherm and chemical speciation analysis of Hg(II) adsorption over oxygen-containing MXene adsorbent. *Chemosphere* **2021**, *278*, 130206. [CrossRef]

37. Cheung, W.H.; Szeto, Y.S.; McKay, G. Intraparticle diffusion processes during acid dye adsorption onto chitosan. *Bioresour. Technol.* **2007**, *98*, 2897–2904. [[CrossRef](#)]
38. Pan, S.Y.; Syu, W.J.; Chang, T.-K.; Lee, C.H. A multiple model approach for evaluating the performance of time-lapse capsules in trapping heavy metals from water bodies. *RSC Adv.* **2020**, *10*, 16490–16501. [[CrossRef](#)] [[PubMed](#)]
39. Galhoum, A.A.; Elshehy, E.A.; Tolan, D.A.; El-Nahas, A.M.; Taketsugu, T.; Nishikiori, K.; Akashi, T.; Morshedy, A.S.; Guibal, E. Synthesis of polyaminophosphonic acid-functionalized poly(glycidyl methacrylate) for the efficient sorption of La(III) and Y(III). *Chem. Eng. J.* **2019**, *375*, 121932. [[CrossRef](#)]
40. Rangabhashiyam, S.; Anu, N.; Giri Nandagopal, M.S.; Selvaraju, N. Relevance of isotherm models in biosorption of pollutants by agricultural byproducts. *J. Environ. Chem. Eng.* **2014**, *2*, 398–414. [[CrossRef](#)]
41. Liu, L.; Huang, Y.; Zhang, S.; Gong, Y.; Su, Y.; Cao, J.; Hu, H. Adsorption characteristics and mechanism of Pb(II) by agricultural waste-derived biochars produced from a pilot-scale pyrolysis system. *Waste Manag.* **2019**, *100*, 287–295. [[CrossRef](#)]
42. Rashad, M.M.; El-Sayed, I.E.; Galhoum, A.A.; Abdeen, M.M.; Mira, H.I.; Elshehy, E.A.; Zhang, S.; Lu, X.; Xin, J.; Guibal, E. Synthesis of α -aminophosphonate based sorbents: Influence of inserted groups (carboxylic vs. amine) on uranyl sorption. *Chem. Eng. J.* **2021**, *421*, 127830. [[CrossRef](#)]
43. Lima, E.C.; Hosseini-Bandegharaei, A.; Moreno-Piraján, J.C.; Anastopoulos, I. A critical review of the estimation of the thermodynamic parameters on adsorption equilibria. Wrong use of equilibrium constant in the Van't Hoof equation for calculation of thermodynamic parameters of adsorption. *J. Mol. Liq.* **2019**, *273*, 425–434. [[CrossRef](#)]
44. Bakather, O.Y.; Zouli, N.; Abutaleb, A.; Mahmoud, M.A.; Daher, A.; Hassan, M.; Eldoma, M.A.; Alasweda, S.O.; Fowad, A.A. Uranium (VI) ions uptake from liquid wastes by Solanum incanum leaves: Biosorption, desorption and recovery. *Alex. Eng. J.* **2020**, *59*, 1495–1504. [[CrossRef](#)]
45. Zhang, Z.; Dong, Z.; Wang, X.; Dai, Y.; Cao, X.; Wang, Y.; Hua, R.; Feng, H.; Chen, J.; Liu, Y.; et al. Synthesis of ultralight phosphorylated carbon aerogel for efficient removal of U(VI): Batch and fixed-bed column studies. *Chem. Eng. J.* **2019**, *370*, 1376–1387. [[CrossRef](#)]
46. Basu, H.; Saha, S.; Pimple, M.V.; Singhal, R.K. Novel hybrid material humic acid impregnated magnetic chitosan nano particles for decontamination of uranium from aquatic environment. *J. Environ. Chem. Eng.* **2019**, *7*, 103110. [[CrossRef](#)]
47. Zhang, X.; Jiao, C.; Wang, J.; Liu, Q.; Li, R.; Yang, P.; Zhang, M. Removal of uranium(VI) from aqueous solutions by magnetic Schiff base: Kinetic and thermodynamic investigation. *Chem. Eng. J.* **2012**, *198–199*, 412–419. [[CrossRef](#)]
48. Elwakeel, K.Z.; Atia, A.A. Uptake of U(VI) from aqueous media by magnetic Schiff's base chitosan composite. *J. Clean. Prod.* **2014**, *70*, 292–302. [[CrossRef](#)]
49. Song, Q.; Ma, L.; Liu, J.; Bai, C.; Geng, J.; Wang, H.; Li, B.; Wang, L.; Li, S. Preparation and adsorption performance of 5-azacytosine-functionalized hydrothermal carbon for selective solid-phase extraction of uranium. *J. Colloid Interface Sci.* **2012**, *386*, 291–299. [[CrossRef](#)] [[PubMed](#)]
50. Son, D.; Cho, S.; Nam, J.; Lee, H.; Kim, M. X-ray based spectroscopic techniques for characterization of polymer nanocomposite materials at a molecular level. *Polymers* **2020**, *12*, 1053. [[CrossRef](#)]
51. Rao Akshatha, S.; Sreenivasa, S.; Parashuram, L.; Raghunath, M.S.; Yogesh Kumar, K.; Madhu Chakrapani Rao, T. Visible-light-induced photochemical hydrogen evolution and degradation of crystal violet dye by interwoven layered MoS₂/wurtzite ZnS heterostructure photocatalyst. *Chem. Sel.* **2020**, *5*, 6918–6926.
52. Hamza, M.F.; Hamad, D.M.; Hamad, N.A.; Abdel Rahman, A.A.H.; Fouda, A.; Wei, Y.; Guibal, E.; El-Etrawy, A.A.S. Functionalization of magnetic chitosan microparticles for high-performance removal of chromate from aqueous solutions and tannery effluent. *Chem. Eng. J.* **2022**, *428*, 131775. [[CrossRef](#)]
53. Grosvenor, A.P.; Kobe, B.A.; Biesinger, M.C.; McIntyre, N.S. Investigation of multiplet splitting of Fe 2p XPS spectra and bonding in iron compounds. *Surf. Interface Anal.* **2004**, *36*, 1564–1574. [[CrossRef](#)]
54. Esfandiari, N.; Kashefi, M.; Mirjalili, M.; Afsharnejad, S. Role of silica mid-layer in thermal and chemical stability of hierarchical Fe₃O₄-SiO₂-TiO₂ nanoparticles for improvement of lead adsorption: Kinetics, thermodynamic and deep XPS investigation. *Mater. Sci. Eng. B* **2020**, *262*, 114690. [[CrossRef](#)]
55. Wang, J.; Ma, X.; Qu, F.; Asiri, A.M.; Sun, X. Fe-doped Ni 2P nanosheet array for high efficiency electrochemical water oxidation. *Inorg. Chem.* **2017**, *56*, 1041–1044. [[CrossRef](#)] [[PubMed](#)]
56. Ritcey, G.M.; Ashbrook, A.W. *Solvent Extraction: Principles and Applications to Process Metallurgy*; Elsevier: Amsterdam, NL, USA, 1984.
57. Awual, M.R.; Suzuki, S.; Taguchi, T.; Shiwaku, H.; Okamoto, Y.; Yaita, T. Radioactive cesium removal from nuclear wastewater by novel inorganic and conjugate adsorbents. *Chem. Eng. J.* **2014**, *242*, 127–135. [[CrossRef](#)]
58. Persson, I. Hydrated metal ions in aqueous solution: How regular are their structures? *J. Pure Appl. Chem.* **2010**, *82*, 1901–1917. [[CrossRef](#)]
59. Shannon, R.D. Revised effective ionic radii and systematic studies of interatomic distances in halides and chalcogenides. *Acta Crystallogr. A* **1976**, *32*, 751–767. [[CrossRef](#)]